Science of the Total Environment 730 (2020) 138888

Contents lists available at ScienceDirect

Science of the Total Environment

journal homepage: www.elsevier.com/locate/scitotenv

Secondary aerosol formation and its linkage with synoptic conditions during winter haze pollution over eastern China

Tianyi Wang, Xin Huang *, Zilin Wang, Yuliang Liu, Derong Zhou, Ke Ding, Hongyue Wang, Ximeng Qi, Aijun Ding

Joint International Research Laboratory of Atmospheric and Earth System Sciences, School of Atmospheric Sciences, Nanjing University, Nanjing 210023, China
Jiangsu Provincial Collaborative Innovation Center of Climate Change, Nanjing 210023, China

HIGHLIGHTS

- Sulfate, nitrate, and ammonium are main contributors to regional haze pollution.
- Vertical and spatial heterogeneity of chemical production due to synoptic weather evolution
- Distinct land-sea difference in nitrate caused by phase equilibrium transition

GRAPHICAL ABSTRACT

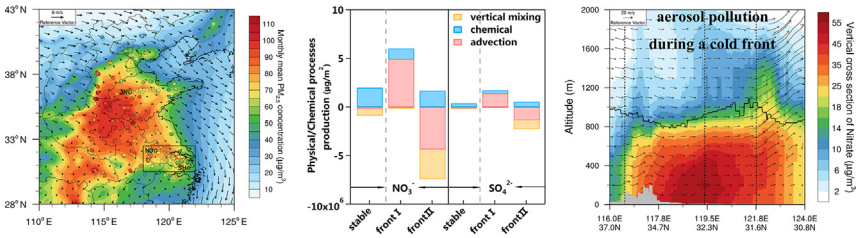

ARTICLE INFO

Article history:
Received 26 March 2020
Received in revised form 19 April 2020
Accepted 20 April 2020
Available online 23 April 2020

Editor: Pingqing Fu

Keywords:
Haze pollution in China
$PM_{2.5}$
SNA
Synoptic conditions
Secondary production

ABSTRACT

Eastern China has been facing severe winter haze pollution due mainly to secondary aerosol. Existing studies have suggested that stagnant weather or fast chemical production led to frequent haze in this region. However, few works focus on the linkage between secondary production of sulfate, nitrate, and ammonium (SNA) and synoptic conditions, and their joint contribution to $PM_{2.5}$. In this study, by combining in-situ measurements on meteorology and aerosol chemical composition at three main cities together with a regional model with improved diagnose scheme, we investigated the chemical formation and accumulation of main secondary composition, i.e. SNA under typical synoptic conditions. It is indicated that SNA did play a vital role in haze pollution across eastern China, contributing more than 40% to $PM_{2.5}$ mass concentration. As most fast developing region, the Yangtze River Delta (YRD) was slightly polluted during stable weather with local chemical production accounting for 61% SNA pollution. While under the influence of cold front, the pollution was aggravated and advection transport became the predominant contributive process (85%). Nevertheless, the chemical production of SNA was notably enhanced due to the uplift of air pollutant and elevated humidity ahead of the cold front, which then facilitated the heterogeneous and aqueous-phase oxidation of precursors. We also found the substantial difference in the phase equilibrium of nitrate over the land surface and ocean due to changes in temperature, ammonia availability and dry deposition. This study highlights the close link between synoptic weather and chemical production, and the resultant vertical and spatial heterogeneity of pollution.

1. Introduction

Fine particles, referred to particulate matter with aerodynamic diameter smaller than 2.5 μm as $PM_{2.5}$, have been proven to pose substantial impacts on climate by perturbing Earth-atmosphere radiation

* Corresponding author at: Joint International Research Laboratory of Atmospheric and Earth System Sciences, School of Atmospheric Sciences, Nanjing University, Nanjing 210023, China.
E-mail address: xinhuang@nju.edu.cn (X. Huang).

https://doi.org/10.1016/j.scitotenv.2020.138888
0048-9697/

balance or acting as cloud condensation nuclei (CCN) and ice nuclei (Lohmann and Feichter, 2005), ecosystems (Carslaw et al., 2010; Held et al., 2002; Kulmala et al., 2004), human health (Harrison and Yin, 2000; Pope III and Dockery, 2006) and visibility (Cao et al., 2012b). Atmospheric $PM_{2.5}$ includes primary components directly released from emission sources and secondary components formed from gaseous precursors through in-situ chemical production and gas-to-particle conversion. It is noteworthy that secondary aerosol has been found to dominate $PM_{2.5}$ mass concentration in many regions across the world (Seinfeld and Pandis, 2016; Zhang et al., 2012b). Sulfate, nitrate and ammonium (SNA) are the predominant inorganic species, accounting for approximately 25%–60% of total $PM_{2.5}$ mass (Chan and Yao, 2008; Pinder et al., 2007; Querol et al., 2004; Yang et al., 2011), and are considered as important contributors to regional visibility deterioration (Huang et al., 2014a; Jung et al., 2009; Wang et al., 2018a; Wang et al., 2015b). Most of SNA aerosols are generated in the atmosphere through oxidation and neutralization of precursor gases: sulfur dioxide (SO_2), nitrogen oxides (NO_x) and ammonia (NH_3) (Wang et al., 2013). SO_2 in the atmosphere is mainly resulted from the combustion of sulfur-containing fuel during residential heating and industry. Industry, power and transportation sectors are the main sources of NO_x emissions. And dominant NH_3 emitters are livestock waste and fertilizer. For the formation of SO_4^{2-}, homogeneous gas-phase oxidation of SO_2, heterogeneous reactions and in-cloud processes, are the primary mechanisms (Huang et al., 2014c; Kunen et al., 1983; Seinfeld and Pandis, 2016; Wang et al., 2006). Nitric acid (HNO_3) is formed through NO_2 oxidized by OH radicals during the daytime and hydrolysis of N_2O_5 at night. (Alexander et al., 2009). H_2SO_4 and HNO_3 are then neutralized by alkaline substances in the atmosphere, mainly NH_3 (Adams et al., 1999; Meng et al., 2015; Meng and Seinfeld, 1994; Pathak et al., 2009).

As the world's largest developing country with rapid industrialization and urbanization, China features a huge amount of coal consumption, resulting in large emission of gaseous precursors SO_2 and NO_x (Dong et al., 2013; Lu et al., 2011; Zhang et al., 2009; Zhang et al., 2012c). Meanwhile, world's top-ranking agricultural production and dense rural population make China a hotspot of NH_3 emission (Huang et al., 2012). Field measurements demonstrated that high levels of gaseous precursors led to significant production of SNA (Guo et al., 2014; Huang et al., 2014b; Wang et al., 2017b; Zheng et al., 2015). Therefore, the concentration and proportion of SNA are both high in China, thus affecting regional air quality and climate change (Cao et al., 2012b; Zhang et al., 2013). Geng et al. (2017) synthesized the in-situ measurement data with satellite-based estimated data and found that the averaged SNA aerosols in northern and central China were most abundant, with the concentration of 46.9 and 43.3 μg/m^3, respectively, while eastern (63%) and northern (61%) China showed the highest fractions. This indicates the serious pollution in China and verifies that the regional distribution characteristics of SNA were consistent with the intensity of urbanization, industrial development and nitrogen fertilizer applications to a large extent (Wang et al., 2017a).

China has been experiencing severe haze events frequently in recent years, especially in winter (Chan and Yao, 2008; Tie and Cao, 2009; Zhang et al., 2012c). The fast increase in SNA has been demonstrated to be one most important contributor to heavy pollution episodes (Tan et al., 2009; Zhang et al., 2013; Zhao et al., 2013b). Many preexisting studies were indicative of the vital role of aqueous-phase oxidation of SO_2 in the rapid increase of SO_4^{2-} under high RH condition during severe haze episodes (Elser et al., 2016; Li et al., 2017; Wang et al., 2014b). Several recent studies have highlighted the aqueous oxidation pathway of SO_2 by NO_2 in SO_4^{2-} formation during the polluted period in China (Cheng et al., 2016; Wang et al., 2016; Xie et al., 2015). The aqueous oxidation pathway of SO_2 by dissolved O_3, H_2O_2, organic peroxides via transition metal ions catalytic or non-catalytic pathways have also been proposed (Zhang et al., 2015b). In addition to emission intensity and secondary formation, formation of severe haze is also strongly affected by regional transport, adverse meteorological condition and synoptic system (Li et al., 2013; Sun et al., 2014; Wang et al., 2014a; Zhang et al., 2016; Zhao et al., 2013b). It has been demonstrated that regional transport is an important factor leading to the severe winter pollution in the super city clusters (Jiang et al., 2015; Tang et al., 2016; Wang et al., 2015a; Xie et al., 2015; Yang et al., 2018; Ying et al., 2014; Zhang et al., 2013; Zhao et al., 2013a; Zheng et al., 2015). Moreover, previous studies have shown that, stable and weak anticyclone synoptic condition at the surface is unfavorable for pollution dispersion (Li et al., 2015a; Liu et al., 2013; Xu et al., 2017). The adverse meteorological variables affecting air quality are often closely interrelated and strongly modulated by the synoptic-scale circulation (Zhang et al., 2012a), including temperature inversion structure, low wind speeds, high humidity and the shallow boundary layer.

Overall, eastern China is facing heavy winter haze pollution under unfavorable meteorological conditions, which is mainly attributed to the high concentration of SNA. Although many studies have suggested that stagnant weather condition or fast chemical production led to frequent haze pollutions in eastern China, the investigation on the linkage between secondary production of SNA and synoptic conditions, and their joint contribution to $PM_{2.5}$ pollution is still very limited. Given a close relationship among the precursor distribution, SNA chemical production and meteorological conditions (i.e. RH, temperature stratification, wind field and their vertical heterogeneity), it is of great importance to clearly show the impacts of different synoptic conditions on secondary aerosol formation and haze accumulation. Therefore, in this study, by combining both the field measurement campaign and WRF-Chem (the Weather Research and Forecasting model coupled with Chemistry) numerical simulations in eastern China from November to December 2017, we comprehensively analyze the regional transport and vertical diffusion of the precursors, the chemical production of SNA as well as its linkage with meteorology under distinct synoptic systems. The rest part of this paper is structured as follows. Section 2 introduces the field campaign and observational data, and the improvement in WRF-Chem model to better diagnose the individual role of various physical and chemical processes. Section 3 first validates the modeling performance using all available measurements, and then analyzes the diagnostic results of chemical formation process of SNA aerosols under two typical winter synoptic systems that controlled eastern China during this campaign. The causes for the difference in the land-sea distribution of NO_3^- chemical formation are also discussed in this section. Finally, conclusions are summarized in Section 4.

2. Data and methodology

2.1. Measurements on meteorology and aerosol chemical composition

To better understand the haze pollution in eastern China, measurements on trace gases (i.e. SO_2, NH_3, NO_2) and aerosol composition were simultaneously conducted at three main cities in eastern China, including Jinan, Nanjing and Shanghai during the time period from 26 November to 26 December 2017. Jinan observation site is located in an urban area of the North China Plain (NCP). The field measurement in Nanjing was performed at the SORPES (Station for Observing Regional Process of the Earth System) station, which has been defined as a suburban site (Ding et al., 2016; Ding et al., 2013c; Nie et al., 2015). And the field measurement in Shanghai was performed at the Fengxian Campus of East China University of Science and Technology representing the rural site (Li et al., 2015b; Qi et al., 2019; Zhang et al., 2017; Zhang et al., 2018). The geophysical locations of these three stations are shown in Fig. 1 for clarity. Water soluble aerosol ions (i.e. NO_3^-, SO_4^{2-}, NH_4^+, Na^+, K^+, Cl^-, Ca^{2+}, Mg^{2+}, etc.) were measured by a Monitor for Aerosols and Gases in ambient Air (MARGA) with a $PM_{2.5}$ cyclone inlet in Jinan and Nanjing. In Shanghai, the mass concentrations of $PM_{2.5}$ species, including organics, sulfate, nitrate, ammonium, and chloride, were measured by Time-of-Flight Aerosol Chemical Speciation

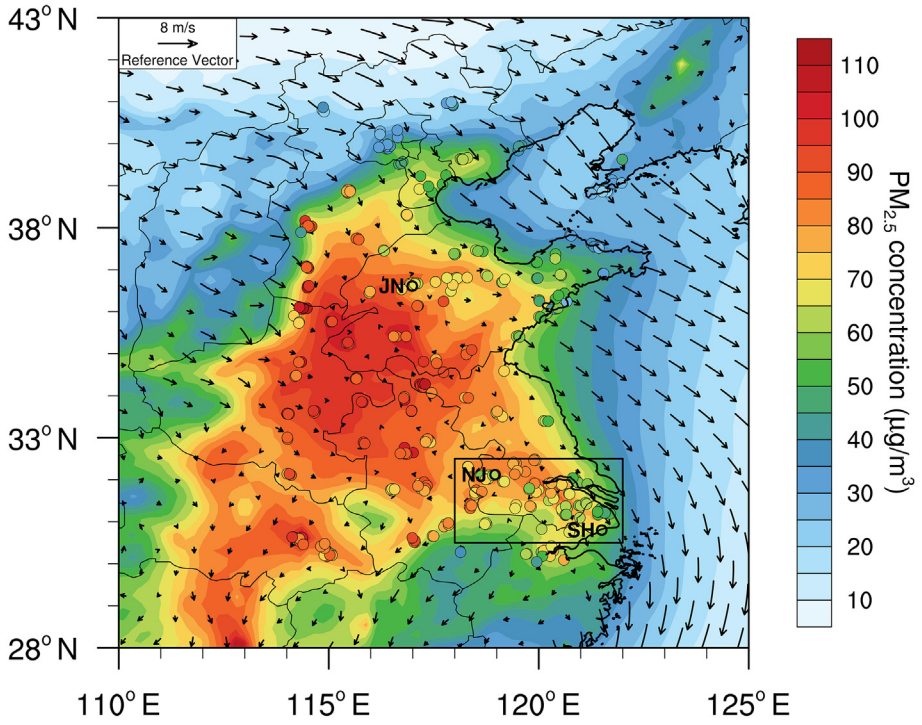

Fig. 1. Spatial distribution of observed (circles) and simulated monthly mean $PM_{2.5}$ concentration and 10-m wind field over eastern China from 26 November to 26 December 2017. The location of Jinan, Nanjing and Shanghai are indicated as black circles.

Monitor (TOF-ACSM). In this work, the sampling sites for Jinan, Nanjing and Shanghai are abbreviated as JN, NJ and SH.

To clearly understand the meteorology and pollution characteristics, several sets of observational data were collected and utilized in this study. Hourly near-surface meteorological parameters such as wind, temperature and RH are recorded by operational automatic weather monitoring stations in Jinan (36.60°N,117.00°E), Nanjing (31.93°N,118.90°E) and Shanghai (31.23°N,121.53°E), which are well quality-controlled and archived at the datacenter of China Meteorological Administration (CMA) (http://www.cma.gov.cn/, last access: September 2019). The observed hourly mass concentration of $PM_{2.5}$ at thousands of ground-based monitoring sites over eastern China are acquired through online access to ambient air monitoring data publicly released by the Ministry of Ecology and Environment (MEE) of People's Republic of China (http://datacenter.mee.gov.cn/, last access: September 2019).

2.2. WRF-Chem improvements and model configurations

The numerical simulations in this study were conducted using the version 3.7.1 of WRF-Chem, which is an online-coupled chemical transport model considering multiple physical and chemical processes, including emission and deposition of pollutants, advection and diffusion, gaseous and aqueous chemical transformation, aerosol chemistry and dynamics (Grell et al., 2011). In highly polluted regions like eastern China, heterogeneous uptake and aqueous reactions have been demonstrated to significantly enhance the secondary production of SO_4^{2-} aerosol, which however have not been well described in current WRF-Chem model. Correspondingly, we improved the aqueous-phase chemistry and heterogeneous module following our previous studies (Huang et al., 2015; Huang et al., 2014c). It is capable of simulating SNA pollution on a regional scale and has been successfully applied in several of our previous studies (Huang et al., 2016; Li et al., 2019; Xu et al., 2018). The model domain in this work was centered at 35°N and 110°E with a grid resolution of 20 km that covered eastern China and the surrounding regions. A total of 35 vertical levels extending from the surface to 50 hPa were utilized in the present study. To better capture the processes in the boundary layer, around 18 layers were placed below 1 km (Wang et al., 2019). The initial and boundary conditions of meteorological fields were constrained by global final analysis (FNL) data with a 1° × 1° spatial resolution produced by the National Centers for Environmental Prediction (NCEP) that updates every 6 h. And National Centers for Environmental Prediction (NCEP) Automated Data Processing (ADP) operation global surface observation and global upper air observational weather data is assimilated by using default nudging coefficients of wind, temperature and moisture to minimize the uncertainties in the reproduction of meteorological fields. The detailed description of model configuration can be found in previous studies (Huang et al., 2016; Huang et al., 2018). The main configurations for the WRF-Chem modeling are listed in Table 1.

To investigate the contributions of each individual physical and chemical process to variations of atmospheric NO_3^- and SO_4^{2-} concentrations, we performed diagnostic analysis in WRF-Chem modeling. The change rate of chemical species concentrations due to the dynamic and chemical production/loss processes are described by a set of mass

Table 1
WRF-Chem modeling configuration options and settings.

Horizontal grid	160 × 180
Grid spacing	20 km
Vertical layers	35
Longwave radiation	RRTMG
Shortwave radiation	RRTMG
Land surface	Noah
Boundary layer	YSU
Microphysics	Lin et al.
Cumulus parameterization	Grell–Deveny
Photolysis	Fast-J
Gas-phase chemistry	CBMZ
Aerosol scheme	MOSAIC

continuity equations given as the following form:

$$\frac{\partial C_i}{\partial t} = -\nabla \cdot (\overline{V} C_i) + \nabla \cdot (K_e \nabla C_i) + \left(\frac{\partial C_i}{\partial t}\right)_{deposition} + \left(\frac{\partial C_i}{\partial t}\right)_{gas-phase\ chemistry} + \left(\frac{\partial C_i}{\partial t}\right)_{cloud\ chemistry} + E$$

where C_i is the concentration of the chemical species to be diagnosed, $\overline{V}$ is the three-dimensional wind velocity vector at each grid point and hence the first term in the right hand denotes advection process; K_e is the eddy diffusion coefficient used to parameterize the subscale turbulent fluxes to present the diffusion process driven by the vertical gradient. The concentration of specific component is also affected by the gas-phase chemistry, in-cloud process, deposition and local emissions (E). In this work, we recorded changes in concentrations due to vertical mixing with dry deposition (vmix), gas-phase and cloud-phase chemistry (chem), and advection (adv, including horizontal and vertical components) at each integration step.

2.3. Lagrangian particle dispersion modeling

To better diagnose the transport and dispersion processes for the episodes, we employed the backward Lagrangian particle dispersion modeling (LPDM) based on HYSPLIT (Stein et al., 2015), following a method developed and evaluated by Ding et al. (2013a). Note that in this study the model was driven by the output meteorological fields of WRF assimilated by observational data as an optimization to achieve finer horizontal resolution in eastern China. For each hour during the study period, 3000 particles were released at 100 m altitude over the selected site and were traced backward for 3 days. The position of particle was calculated considering the mean wind field and turbulent transport within the PBL after being released from the receptor point. The residence time of particles below the 100 m level called footprint retroplume was also used to understand the contribution from potential source regions (Ding et al., 2013c).

3. Result and discussion

3.1. General meteorological and pollution characteristics and model evaluation

The model representation on spatial pattern of $PM_{2.5}$ pollution was first evaluated in Fig. 1, which presents the simulated and observed monthly averaged $PM_{2.5}$ concentration and simulated 10-m wind over eastern China from 26 November to 26 December 2017. It shows that the model did well capture the spatial distribution of $PM_{2.5}$, including high levels of $PM_{2.5}$ concentrations over southern Hebei, Henan, Shandong and Hubei Province. Additionally, the Yangtze River Delta (YRD) also witnessed heavy haze pollution along the city clusters from Nanjing to Shanghai, especially in areas with extremely low wind speed.

As mentioned in Section 2, we conducted simultaneous measurements on both meteorology and aerosol composition at three representative cities. These observational data at Jinan, Nanjing and Shanghai from the north to the south were also employed to further validate the model. The model-simulated daily mean surface meteorological parameters, $PM_{2.5}$ and its major secondary inorganic components concentrations were compared with corresponding observations at these three cities. Fig. 2 compares the daily averaged 10-m wind speed, 2-m temperature, $PM_{2.5}$, SO_4^{2-}, NO_3^- and NH_4^+ concentrations between the simulations and observations from 26 November to 26 December 2017. The simulation of temperature was relatively more accurate with a correlation of 0.96 and a RMA slope of 0.98, but the simulated values were sometimes slightly lower, which might be related to the time lag between the actual urbanization process and the land-use data over complex terrains in the parameterization scheme used by the model (Dandou et al., 2005). The wind speed was significantly overestimated in all three cities with the RMA slope reaching 1.33. A high positive bias in wind speed was also reported by several other studies using WRF-Chem (Matsui et al., 2009; Moelders et al., 2012; Tuccella et al., 2012; Zhang et al., 2010). This overestimation probably resulted from the underestimation of the frictional weakening effect of the actual urban underlying surface type on the wind field, which was similar to the temperature simulation. It may also result from the unresolved topographical features in surface drag parameterization and the coarse resolution of the domain (Cheng and Steenburgh, 2005; Yahya et al., 2015). In addition, the WRF model may have systematic deviations in simulating wind speed in the lower atmosphere. The correlation coefficients for $PM_{2.5}$, SO_4^{2-}, NO_3^- and NH_4^+ concentrations were found to be 0.75, 0.50, 0.77, and 0.72, respectively. This indicated that the model successfully reproduced the day-to-day variations of pollutants concentrations. Although the model performance for pollutants was satisfactory, biases still existed. The biases can be probably attributed to errors in meteorology, large uncertainties of emission inventory, relatively coarse model grid size, and incomplete treatments of atmospheric chemistry (Harris et al., 2013; Zhang et al., 2015a).

Overall, the evaluations suggested that the model generally well simulated the spatial and temporal variations of meteorological variables and particle pollutants, verifying that the model can well present the meteorological and aerosol spatiotemporal variation in eastern China during this campaign.

3.2. Pollution episodes under distinct synoptic weather conditions

Fig. 3 displays the time series of hourly 2-m temperature, $PM_{2.5}$ and SNA concentrations at three cities during the month. It should be noted that the analysis of the following part is based on the model simulation results unless otherwise specified, as the model performance has been evaluated previously. The concentration of pollutants in winter showed a certain periodic variation. After accumulating for a period of time under the control of high pressure, the cold front formed by the encounter of cold air in front of the Siberian high pressure and the warm air in the downstream, resulting in the significant removal of pollutants during the southward movement, accompanied by a certain degree of cooling. It can also be seen that in several pollution episodes, the time of $PM_{2.5}$ concentration peak in the three cities was delayed from the north to the south, indicating the regional transport process of air pollutants. The most polluted period appeared at the end of the month from 23 to 24 December 2017. A burst growth of $PM_{2.5}$ pollution successively occurred in Jinan, Nanjing, and Shanghai in a short term, accompanied by strong north-west wind. The peaks of $PM_{2.5}$ concentration reached Jinan, Nanjing, and Shanghai at 18:00 LT 23 December, 09:00, and 12:00 LT 24 December, with the maximum concentrations of 281.4, 299.5, 297.4 μg/m^3, respectively, and a 3 h delay from Nanjing to Shanghai. This process indicated that a strong north-westerly flow carries polluted air masses across the YRD region (Fig. 4c and d). By the time of 18:00 LT 24 December, the $PM_{2.5}$ concentrations in three cities were basically reduced to the minimum. The city with the largest monthly mean SNA fraction (46%) in $PM_{2.5}$ was Shanghai, with the fractions of SO_4^{2-}, NO_3^- and NH_4^+ being 13%, 22%, 11%, respectively. In Jinan, SNA aerosols accounted for 41% of $PM_{2.5}$ mass, of which SO_4^{2-}, NO_3^- and NH_4^+ contributed 6%, 25% and 10%, while the averaged fractions were 44%, 8%, 26% and 10% for respective SNA in Nanjing, which were comparable with those observed in eastern China (Cao et al., 2012a; Huang et al., 2014b; Ming et al., 2017).

Local meteorology, controlled by synoptic conditions, could have "deterministic impacts" on air pollution levels (Xu et al., 2011). Combined with the sea level pressure field shown in Fig. 4, the head of the cold air masses reached Jinan at 18:00 LT 23 December (Fig. 4c). The YRD region was situated in front of a ridge and behind a trough at 500 hPa geopotential height field, corresponding to the weak low-pressure system (cyclone) on the ground. The warm and humid

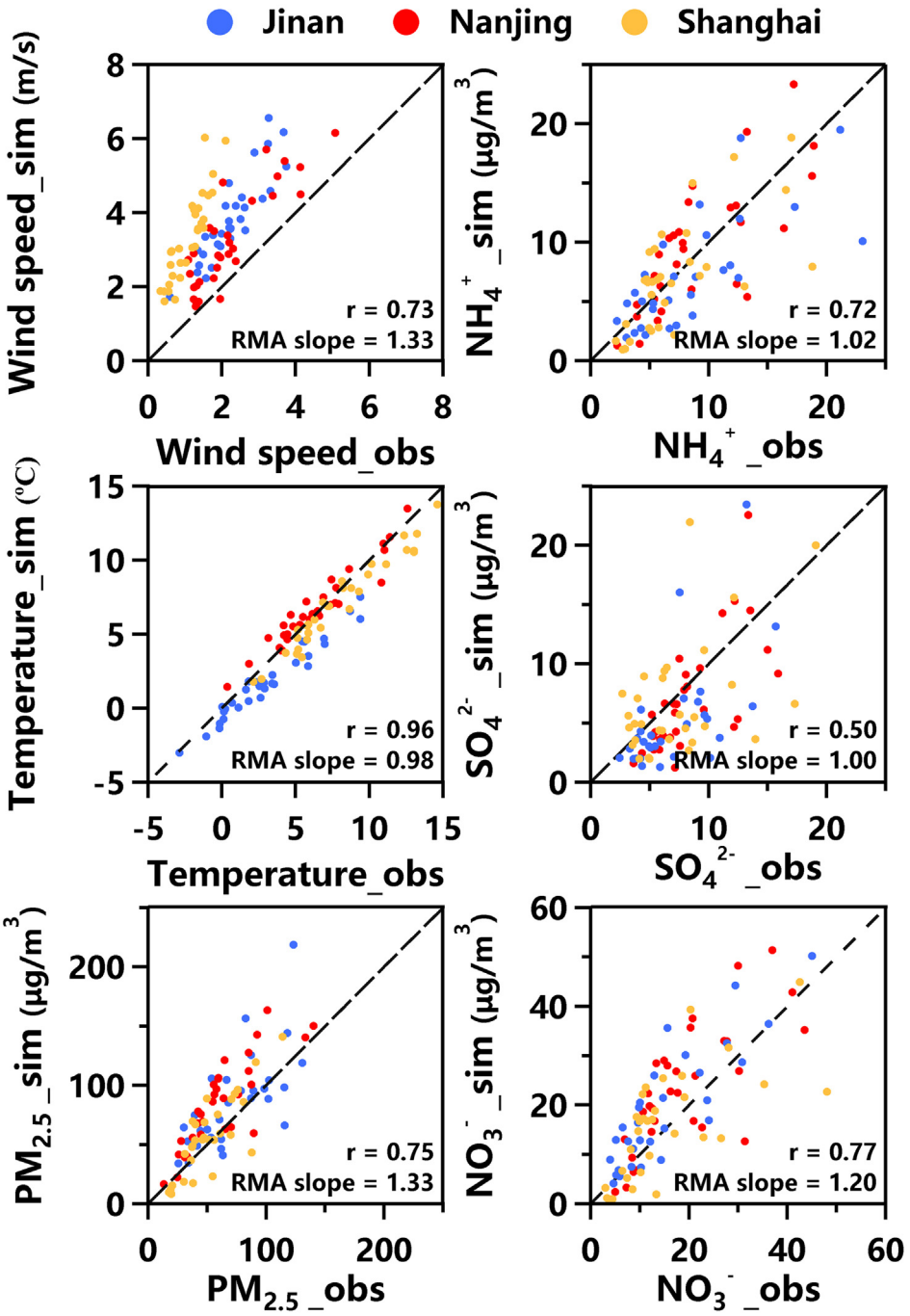

Fig. 2. Scatter plots of simulated daily mean meteorological parameters, $PM_{2.5}$ and its major chemical composition (SO_4^{2-}, NO_3^- and NH_4^+) versus observed values among Jinan, Nanjing and Shanghai during 26 November to 26 December 2017.

airflows of southwest were easy to accumulate in the front part of the low pressure, which made the air masses warmer to form the inversion layer. The inversion intensity gradually increased with the increasing humidity of the ground (Zhu et al., 2016). The observed vertical profile of the temperature showed a large temperature difference from the upper level to the ground. At that moment, a southerly wind prevailed in the YRD region. Twenty hours later, the cold front moved southeastward to the coastal areas downstream of YRD (Fig. 4d). The sea level pressure field showed that there were large pressure gradients at the front of the cold front, with the prevalence of wind direction shifting to the north-west over YRD region in the meanwhile, which favored the transport of air pollutants from the upstream region to the YRD area (Kang et al., 2019). After the cold front transited, under the sharp pressure gradient, the Siberian anticyclone brought effective convection and strong northerly wind carrying dry and clean air to YRD, which resulted in a sharp drop of $PM_{2.5}$ concentrations. Then, synoptic patterns in YRD were characterized by the high-pressure system or uniform pressure field with light horizontal winds (Fig. 4a and b). Under such conditions, it was unfavorable for the horizontal advection and the vertical mixing process within the boundary layer (Zhu et al., 2010). Therefore, particulate matter gradually accumulated in the YRD region under such stable weather condition. In order to compare with the influence of cold front, this study selected the stable period controlled by the high pressure just after the cold front from 25 to 26 December 2017 as case 1, in which the average $PM_{2.5}$ concentrations of Jinan, Nanjing and Shanghai were 61.0, 76.9, and 90.4 μg/m^3, respectively. As shown in

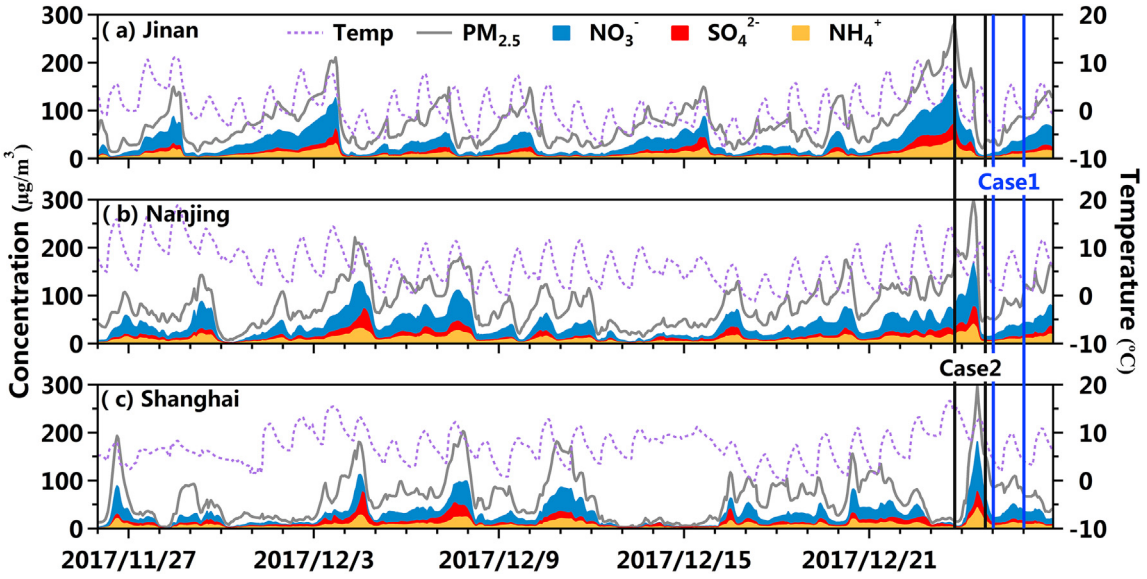

Fig. 3. Time series of simulated hourly 2-m temperature, $PM_{2.5}$ and its major chemical composition (SO_4^{2-}, NO_3^- and NH_4^+) at (a) Jinan, (b) Nanjing and (c) Shanghai from 26 November to 26 December 2017. The blue and black rectangles indicated the selected case1 and case2 under different synoptic situation, respectively.

Fig. 4c and d, Jinan, Nanjing, and Shanghai were at the edge of the high-pressure center. Subsidence was prevalent in high-pressure controlled areas, where pollutants were prone to build up near the ground, indicating that pollution was more likely to be originated from local sources. For case 2, the strong synoptic systems, i.e., the cold front intruded into the YRD region from 18:00 LT 23 to 18:00 LT 24 December 2017, with the averaged $PM_{2.5}$ concentrations of 162.3, 189.2, and 110.1 μg/m^3 in Jinan, Nanjing and Shanghai during this period, respectively.

To identify the sources of these particles and to investigate their transport pathways, we conducted LPDM for case 1 and 2 and showed the footprint retroplumes (Fig. 5). Fig. 5a suggested that the air masses reaching SORPES during case 1 were mainly local and short-distance air masses from the southwest, reflecting the local source emissions and accumulation of pollutants. For case 2, the SORPES site was first affected by the air masses from the Hangzhou Bay in the southeast and the southwest air mass, and then the dominant airflow gradually shifted to the north-west (Fig. 5b). The transported pollutants mixed with local emissions accumulated continuously to the maximum until the cold front passed through. The strong winds diluted the concentration of pollutants. The stability of the atmosphere was destroyed because of the invasion of cold air, forcing the boundary layer to rise and strengthening atmospheric turbulence diffusion, which eventually led to a rapid decrease in the concentration of ground pollutants (Zhou et al., 2018).

A process diagnostic analysis technique, as elaborated in Section 2.2, was applied to disentangle each individual contribution from different physical or chemical processes to aerosol variations over the YRD region (from 118 to 122°E, 30.5 to 32.5°N, marked in Fig. 1), including the south of Jiangsu province, Shanghai, and the north of Zhejiang province, since the frontal zone was smaller than the entire YRD region. Fig. 6 shows the averaged contributions from chemical, vertical mixing with dry deposition, and advection transport processes on the concentrations of NO_3^- and SO_4^{2-} under 500 meter in altitude during these two cases. Considering that the advection transport changed from positive contribution to negative contribution after the cold front passed through, case 2 was divided into two time periods by the time when the pollutants concentration reached the maximum. In recent years, under the regulation of policies, SO_2 emission reduction has achieved remarkable accomplishment. At the same time, China has gradually transitioned to the situation where NO_3^- is dominant in secondary inorganic aerosols of $PM_{2.5}$ associated with the substantial reduction of SO_2 in the cold season (Ding et al., 2019). This can also be seen from the diagnostic result that the concentration of NO_3^- was significantly higher than SO_4^{2-}. Under the stable weather situation, for NO_3^- and SO_4^{2-}, the absolute mean contribution values of vertical mixing process and chemical formation process were comparable, but chemical formation process contributed more to the increase of SNA concentration. Probably because of the prevailing subsidence under high-pressure control, stable atmospheric stratification was unfavorable for the long-range transport of pollutants, while the stagnant weather with stronger radiation promoted photochemical reactions. When eastern China was affected by the cold front, namely stage I (18:00 LT 23 to 08:00 LT 24 December) in the period before the arrival of the cold front, the center of the YRD was located ahead of the frontal zone at this time, and the contribution of advection transport processes to aerosol concentrations was positive. In the stage II (08:00 to 18:00 LT 24 December), after the cold front passed through, the pollutants were removed by strong winds, and the contribution of advection transport processes became negative. However, the absolute contributions of advection transport processes in both stages were much larger than that of chemical formation process, by approximately 3.5 times. The vertical mixing process with dry deposition and advection transport processes were comparable under the influence of cold front, which was consistent with the results of processes diagnostic analysis on $PM_{2.5}$ in Qingdao based on the simulation of CMAQ (Gao et al., 2020). It is worth noting that the contribution of vertical mixing increased significantly after the cold front passed through, indicating that the polluted air mass was lifted to higher altitude by the upward motion ahead of the frontal zone, resulting in the enhancement of vertical mixing. The production of gaseous H_2SO_4 and HNO_3 could reflect the gas-phase oxidation process with obvious diurnal variation patterns, and the production rates increased during case 2 (Fig. 6b and c). Although the advection transport processes contributed the most in case 2, the contribution of chemical formation part was still not negligible. Therefore, in next sections, chemical formation of SNA aerosols under different synoptic systems was analyzed in detail.

3.2.1. Case 1: SNA formation under stable weather condition

Fig. 7 shows the average spatial distribution of surface wind field and column concentrations during case 1. After the cold front event, aerosol particles began to accumulate with low wind speeds under the stagnant weather condition over YRD region. The relatively high levels of NO_3^- column concentration were evenly distributed in the YRD areas, with

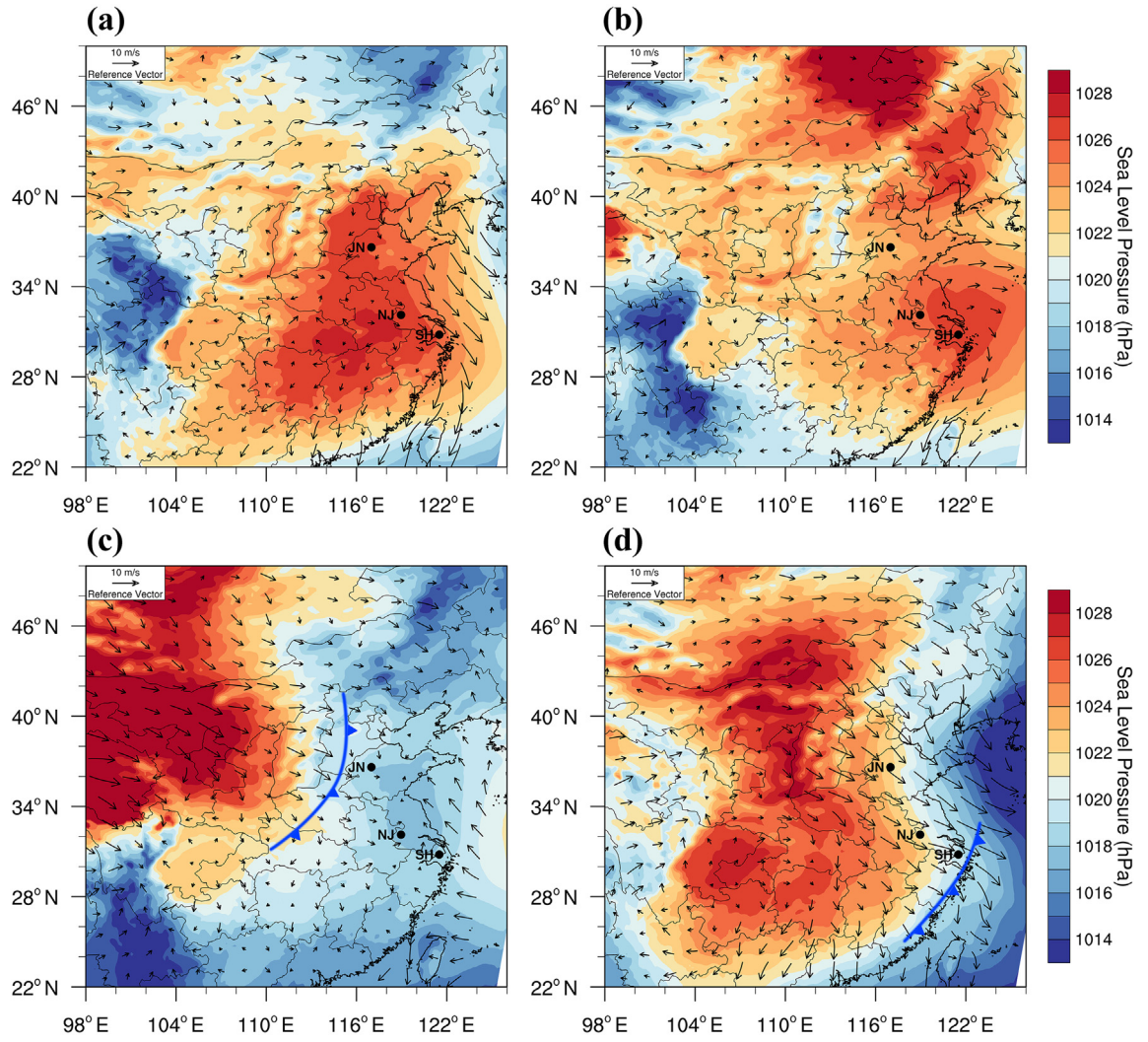

Fig. 4. Sea level pressure field over the YRD region at: (a) 00:00 LT on 25 December, (b) 00:00 LT on 26 December, (c) 18:00 LT on 23 December, (d) 12:00 LT on 24 December. Panels (a) and (b) are the stable weather conditions under high pressure control as case 1, and panels (c) and (d) are under the influence of the cold front system as case 2. The surface position of the cold front is marked with the symbol of a blue line of triangles pointing in the direction of travel in panels (c) and (d). The location of Jinan, Nanjing and Shanghai are indicated as black points.

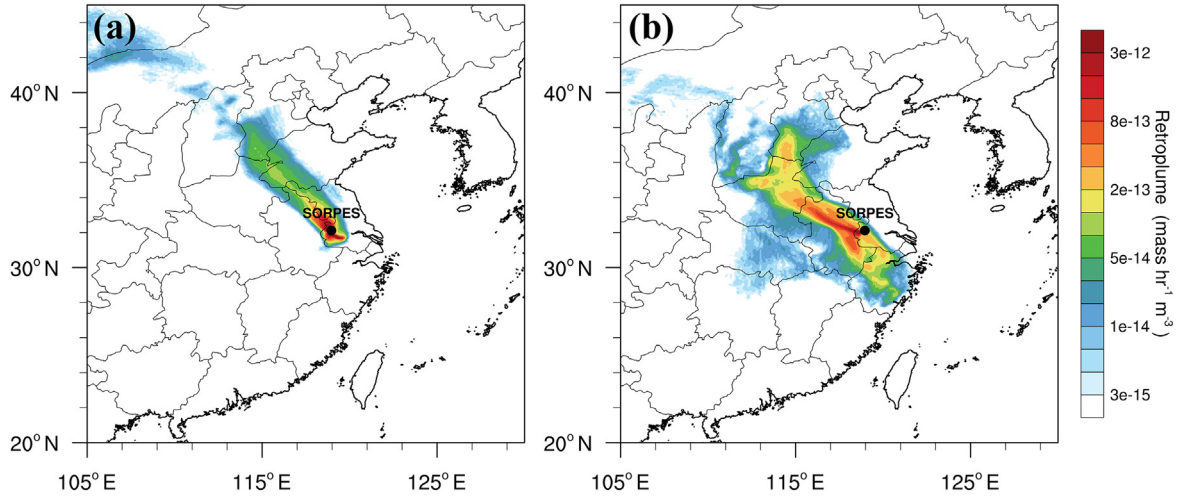

Fig. 5. The averaged retroplumes (i.e., 100 m footprint) based on 3-day backward Lagrangian particle dispersion modeling during (a) case 1, and (b) case 2. Note: Black dot gives the location of SORPES station. The method of calculating the footprint was developed by Ding et al. (2013a), based on the Hybrid Single-Particle Lagrangian Integrated Trajectory (HYSPLIT) model (Stein et al., 2015).

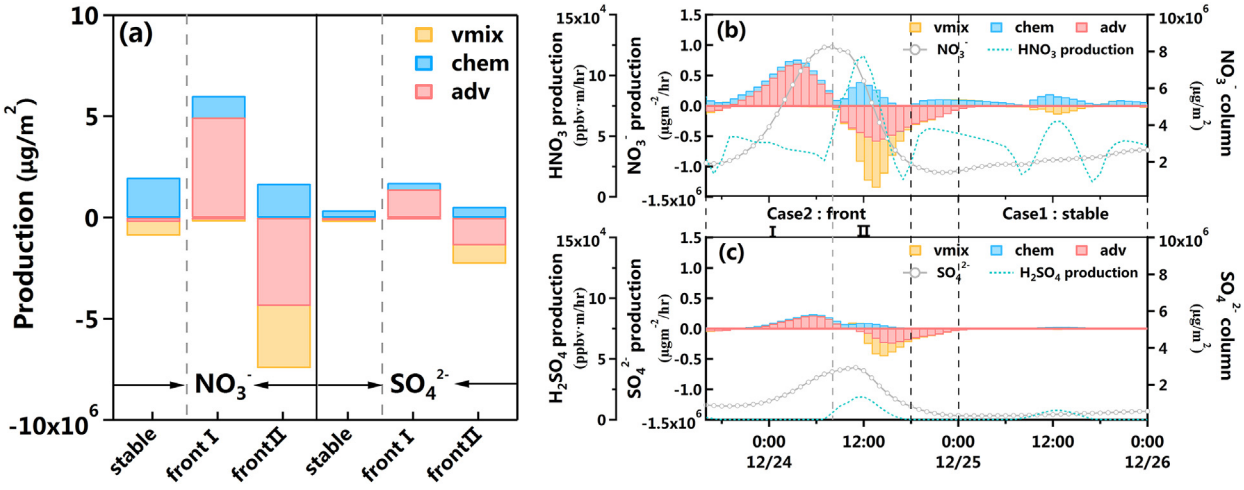

Fig. 6. (a) The total contribution of physical/chemical processes (vmix = vertical mixing with dry deposition; chem = chemical production; adv = horizontal and vertical advection) over the center of the YRD (118°E-122°E, 30.5°E-32.5°E, marked in Fig. 1) to NO_3^- and SO_4^{2-} column concentrations in the near surface (within 500 m) during case 1 and case 2. (b) Time series of column concentrations and contributions of NO_3^- from different processes in the near surface (within 500 m) from 18:00 LT 23 December 2017 to 00:00 LT 26 December 2017, covering the time periods of case 1 and case 2. (c) Same as (b) but for SO_4^{2-}. Note that case 2 is divided into two stages, stage I is before the arrival of the cold front from 18:00 LT 23 to 08:00 LT 24 December 2017, and stage II is after the arrival of the cold front from 09:00 LT to 18:00 LT 24 December 2017.

an average value of about 18.4 mg/m^2 (Fig. 7a), while the SO_4^{2-} column concentrations were slightly higher in YRD region, about 19.9 mg/m^2, and higher in the central region (Fig. 7b). During this period, the distribution of contribution from chemical production process to NO_3^- column corresponded to the distribution of the NO_3^- column concentration, with the average value of about 14.1 mg/m^2, of which the contribution in city clusters near the coastline around Shanghai was slightly larger (Fig. 7c). High concentrations of the gaseous precursor NO_x accompanied by relatively strong photochemical activities in this region were responsible for the larger NO_3^- production (Fig. S1a and S1c). For SO_4^{2-}, the relatively larger contribution of chemical production process appeared in the area around Jinan and the city clusters along the Shanghai-Nanjing axis over the YRD region due to concentrated SO_2 as well as higher relative humidity (Fig. S1d and S1f), with the averaged contribution being approximately 3.2 mg/m^2 (Fig. 7d). The stagnant weather with stronger radiation favored photochemical reactions, and the RH near coastline was relatively high, thus facilitating the gas-phase and aqueous-phase reactions of NO_3^- and SO_4^{2-} production over the YRD.

In general, under the stagnant weather condition of case 1, the distribution of NO_3^- and SO_4^{2-} column concentration in YRD area was consistent with that of contribution from chemical formation process in the YRD region in terms of spatial distribution. Quantitatively, chemical production was the main process contributing to the concentration of SNA, which contributes more than 60%. And it can be found that the YRD region would not be at the level of heavy pollution, while the concentration of secondary inorganic aerosols mainly came from the contribution of gas precursors generated by local source emissions through chemical conversion process.

Since case 1 featured locally-formed secondary pollution under stagnant wind, we mainly focused on boundary layer evolution and its impacts on the vertical heterogeneity of SNA formation. To figure out the characteristics of vertical structure of SNA and its precursors in case 1, temporal variations of NO_3^-, SO_4^{2-} and their corresponding precursors and chemical production contribution profiles are illustrated in Fig. 8. SORPES was selected as the representative for further analysis considering that local emissions dominated in this case. High concentrations of aerosols largely accumulated in the near ground, and the concentration increased gradually after the noon. Under the stable condition of low wind speed controlled by high pressure, pollutants emitted from local sources began to accumulate again at the SORPES station (Ding et al., 2013b; Ding et al., 2013c; Shen et al., 2018).

As shown in Fig. 8a, the NO_3^- concentration increased after the sunrise, which was mainly attributed to the fact that gaseous HNO_3 rose through photochemical reactions as solar radiation getting stronger. NO_3^- concentration began to increase obviously due to the large amount of NO_x emitted during the morning rush hours and the enhancement of photochemical reactions (Liu et al., 2019). Since the temperature had not risen significantly at this time, the maximum values of the chemical production contribution in case 1 occurred during 10:00–12:00 LT, and the height at which the max value appeared gradually increased with the development of boundary layer (Huang et al., 2018; Wang et al., 2018b). The boundary layer development led to much stronger vertical diffusion of NO_3^- in the afternoon (Ding et al., 2016; Zhang et al., 2010). Therefore, the positive contribution of gas-phase chemical production and the negative contribution of vertical dilution were partly offset, which weakened the net chemical contribution in the afternoon. With the fully developed boundary layer, intense turbulent diffusion gave rise to the well-mixed pollutants. Abundant NH_3 near the ground surface promoted the conversion from gaseous nitric acid to particulate NO_3^- aerosol, leading to fast increase in NO_3^- aerosol during daytime near surface. Above the boundary layer, less NH_3 availability hindered the neutralization of HNO_3 and subsequent NO_3^- aerosol formation. That was why HNO_3 concentration peaked near the top of the boundary layer and NO_3^- chemical production showed a sharp drop at higher altitude (Fig. 8c).

During the nighttime, NO_3^- aerosol still gradually concentrated, which might be related to the hydrolysis of dinitrogen pentoxide (N_2O_5). The equilibrium of gas-particulate partition of NO_3^- is highly temperature-dependent, and NO_3^- tends to exist in the particulate phase when the temperature is low (Ansari and Pandis, 2000; Seinfeld and Pandis, 2016). The heterogeneous hydrolysis of N_2O_5 – a reaction product of NO_2 and nitrate radical, is believed to be the dominate pathway to form particulate NO_3^- (Brown et al., 2003), which is also supported by the evidence found in previous study at the SORPES station (Sun et al., 2018). So nitric acid can form via the reaction between N_2O_5 and water vapor, or via the heterogeneous hydrolysis on the wet surface to form the particulate NO_3^- directly (Thornton et al., 2003; Wang et al., 2017a; Wen et al., 2018). But values of chemical contribution to NO_3^- concentration in the nighttime were comparatively small. The temporal evolution of SO_4^{2-} was similar to that of NO_3^-, accumulating gradually after the noon (Fig. 8b). However, unlike NO_3^-, SO_4^{2-} formation predominantly occurred in daytime due mainly to the photochemical formation of H_2SO_4. Vertically, less preexisting aerosol

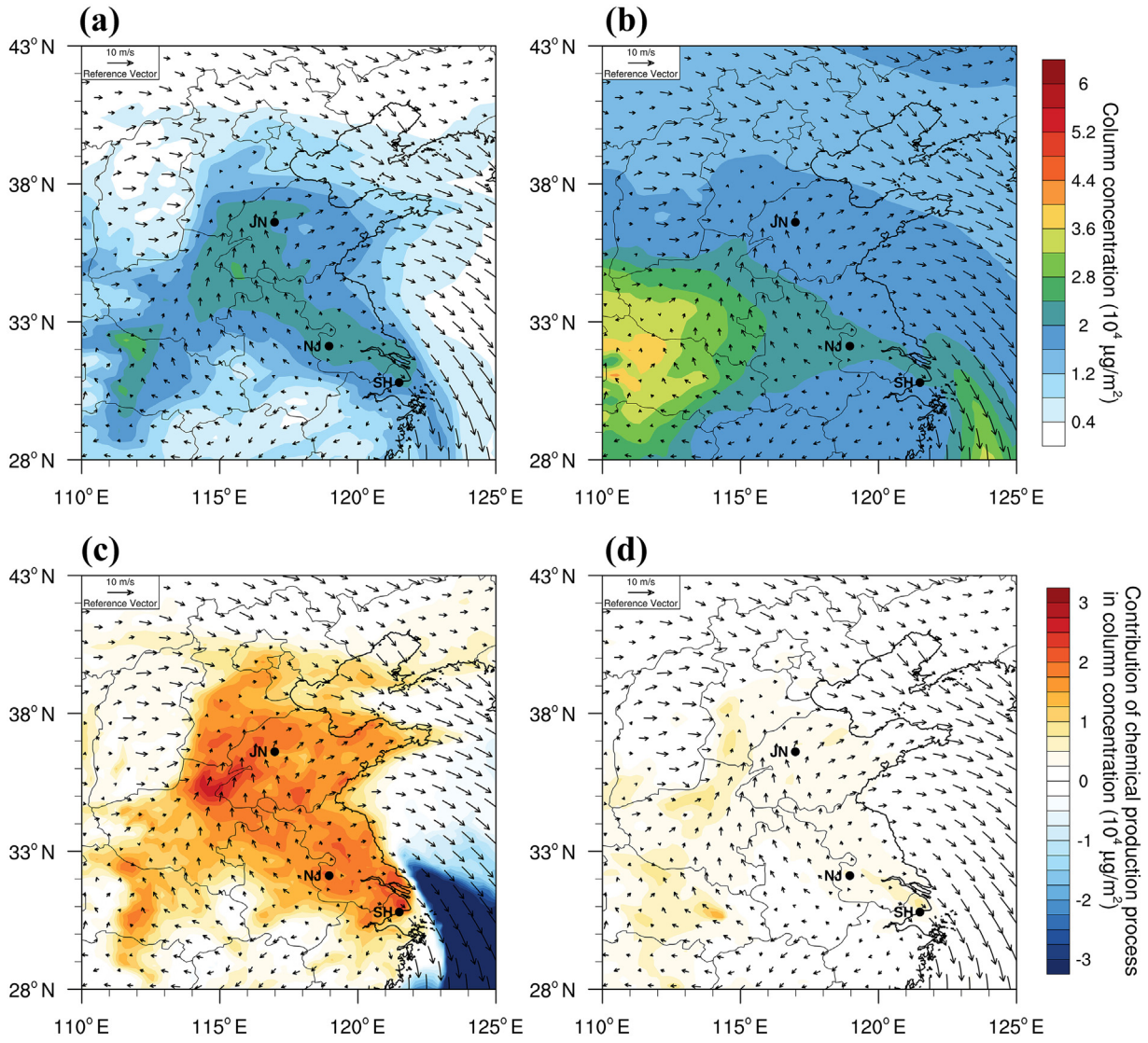

Fig. 7. Spatial distribution of the averaged column concentration during case 1. (a) NO_3^- column, (b) SO_4^{2-} column, (c) Column of NO_3^- from chemical production process, (d) Column of SO_4^{2-} from chemical production process. The location of Jinan, Nanjing and Shanghai are indicated as black points.

and higher radiation flux made H_2SO_4 reach the maximum at the top of PBL (Fig. 8d).

Overall, under the stagnant condition, the variations of NO_3^- and SO_4^{2-} were mainly driven by gaseous precursors, photochemical activities, conversion rate, air temperature, RH, boundary layer dynamics at local scale (Cheng et al., 2016; Guo et al., 2017; Li et al., 2017; Seinfeld and Pandis, 2016; Xie et al., 2015; Zhang et al., 2007). High concentrations of aerosols and their gaseous precursors appeared near the surface, while HNO_3 and H_2SO_4 mainly appeared above the top of the PBL. Compared with those inside the PBL, lower preexisting aerosol limited condensation sinks and higher oxidizing capacity in the free troposphere favored the photochemical oxidation and accumulation of HNO_3 and H_2SO_4 (Qi et al., 2019). In addition, it was also highly possible that as NH_3 accumulated mostly near the surface, HNO_3 and H_2SO_4 were much easily neutralized by NH_3 near the ground surface.

3.2.2. Case 2: formation of SNA under the effect of cold front

Case 2 is an episode significantly influenced by a typical synoptic system in winter – the cold front. Fig. 9 gives the average spatial distribution of surface wind field and column concentrations during that case. Strong wind accompanied by high concentrations of $PM_{2.5}$ in winter favored the long-range transport of aerosols from polluted North China Plain (NCP) to the YRD region. High NO_3^- and SO_4^{2-} loadings covered most part of the YRD and Shandong Province, with the maximum values reaching 63.3 and 45.8 mg/m^2, respectively. There were two distinct bands of high-value areas: one was from the west of Shandong Province to the city clusters along the Shanghai-Nanjing axis over the YRD region, and the other was along the coastline of Jiangsu Province (Fig. 9a and b). Such belt distribution was mainly attributed to the evolution of wind, starting along the north-west direction and then changing to the westerly direction, which suggested the pathway of cold front. Correspondingly, the high SNA concentration was distributed on the moving path of the cold front. The distributions of chemical production contribution to NO_3^- and SO_4^{2-} corresponded to their column concentration distributions, with the average contributions of about 14.7 and 8.7 mg/m^2, respectively (Fig. 9c and d). Through the transport of pollutants by the cold front, the pollution was gradually aggravated and the photochemical reactions were suppressed. However, higher RH facilitated the aqueous-phase reaction and heterogeneous uptake, which enhanced the formation of secondary aerosol in case 2 (Fig. S2). Generally, YRD was less polluted under stable conditions than that under the influence of cold fronts. When comparing the contribution of chemical production to SNA, the chemical production under stable weather (61.3%) contributed more to the column concentrations than

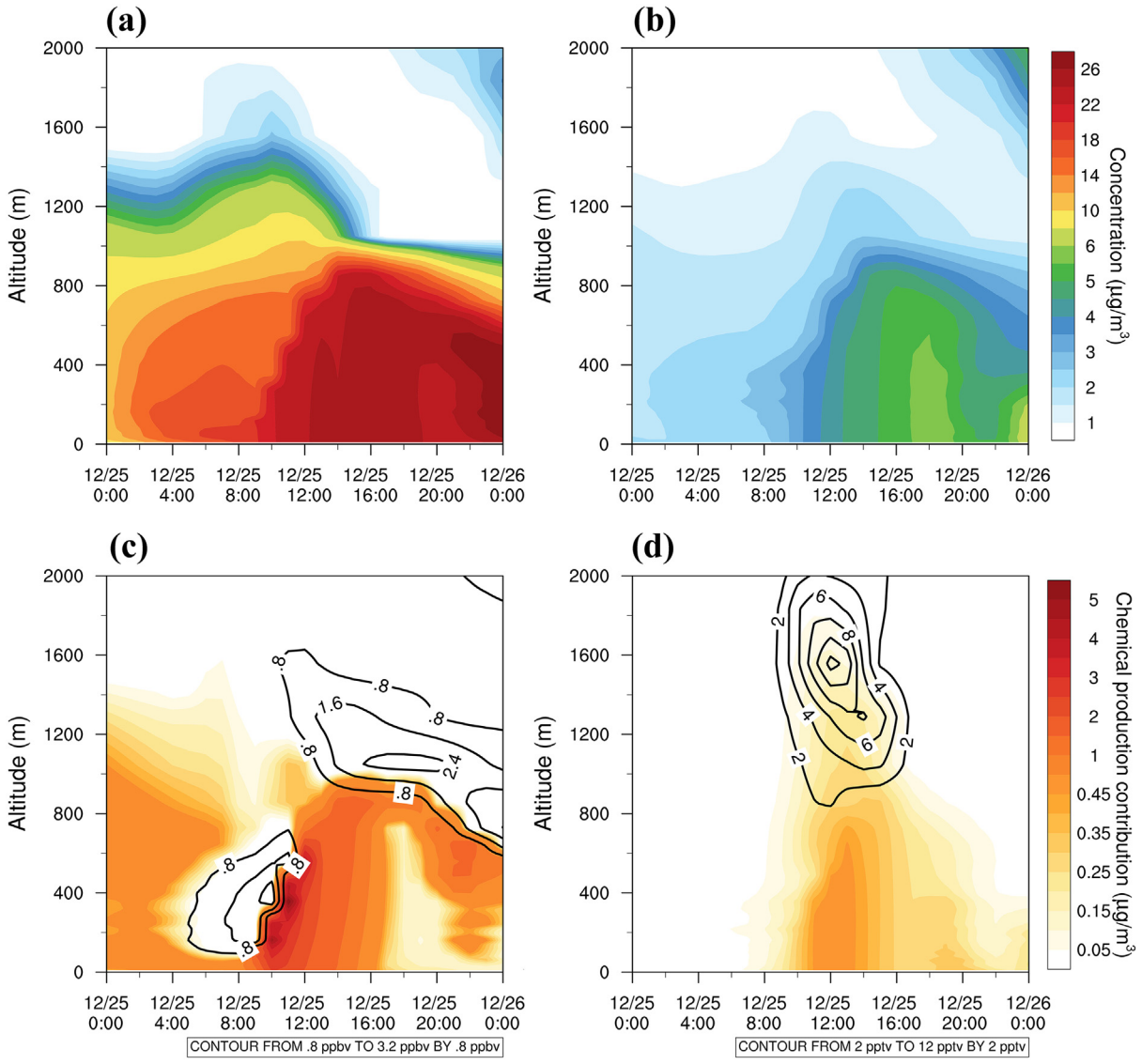

Fig. 8. Temporal evolutions of the vertical profile for (a) NO_3^-, (b) SO_4^{2-}, (c) chemical production rate of NO_3^- (color-filled contours) overlaid by HNO_3 (black contours), (d) chemical production rate of SO_4^{2-} (color-filled contours) overlaid by H_2SO_4 (black contours) at the SORPES site during case 1.

that under the influence of cold front (14.8%) in terms of relative contribution ratio, but the absolute values were the opposite.

To get a better insight into the chemical production of SNA during case 2, cross section of averaged pollutants and corresponding chemical production contribution profiles along the transport pathway of cold front are shown in Fig. 10. As shown the high concentration SNA dominated the entire region in the whole PBL, indicating that the cold front was accompanied by SNA transport. The vertical extent of the SNA concentrations reached 1.6 km, significantly higher than the mean boundary layer height. Therefore, the vertical transport of SNA was considered to be caused by the upward motion in front of the cold front system, rather than the vertical turbulent mixing in the PBL. When the cold front reached the YRD, the warm and polluted air mass ahead of the frontal zone was lifted up to the free troposphere (Ding et al., 2009; Liu et al., 2003; Zhou et al., 2018). The high concentration center of NO_3^- and SO_4^{2-} appeared between 200 and 400 m, higher than that in the stable period (mainly near the ground), which also proved that the cold fronts had lifting effect (Fig. 10a and b). The chemical formation mainly occurred within the PBL, from the near ground to the height of 600 m. And the large values of chemical contribution to NO_3^- and SO_4^{2-} were both distributed in the downwind region along the city clusters from Nanjing to Shanghai, which included two parts, that is, the chemical conversion of the local emissions and the transported gaseous precursors from NCP. Moreover, the RH profiles showed that the downstream areas were more conducive to aqueous-phase and heterogeneous reactions (Fig. 10c and d). We selected 03:00 LT 24 December in Fig. 11 to show the instantaneous vertical distribution when the cold front was located between Jinan and Nanjing. It is evident that the concentration of NO_3^- and SO_4^{2-} and the contribution from chemical formation were distributed both in and above the boundary layers, reflecting the rise along the circulations ahead of cold fronts.

3.3. Substantial land-sea difference of NO_3^- chemical production

From (c) and (d) of Figs. 7 and 9 in the spatial pattern and (c) and (d) of Fig. 10 in the vertical distribution, it can be found that the total contribution of chemical formation to NO_3^- concentration was clearly demarcated along the coastline, that is to say, there was a significant difference in land-sea distribution, with positive contribution on land and negative contribution at sea. However, chemical formation process contributed positively to SO_4^{2-} and there was no obvious difference in land-sea distribution. Considering that the formation process of SO_4^{2-} is irreversible, the gas-particulate partition of NO_3^- is a reversible equilibrium process, which is affected by temperature, RH and other factors. So we

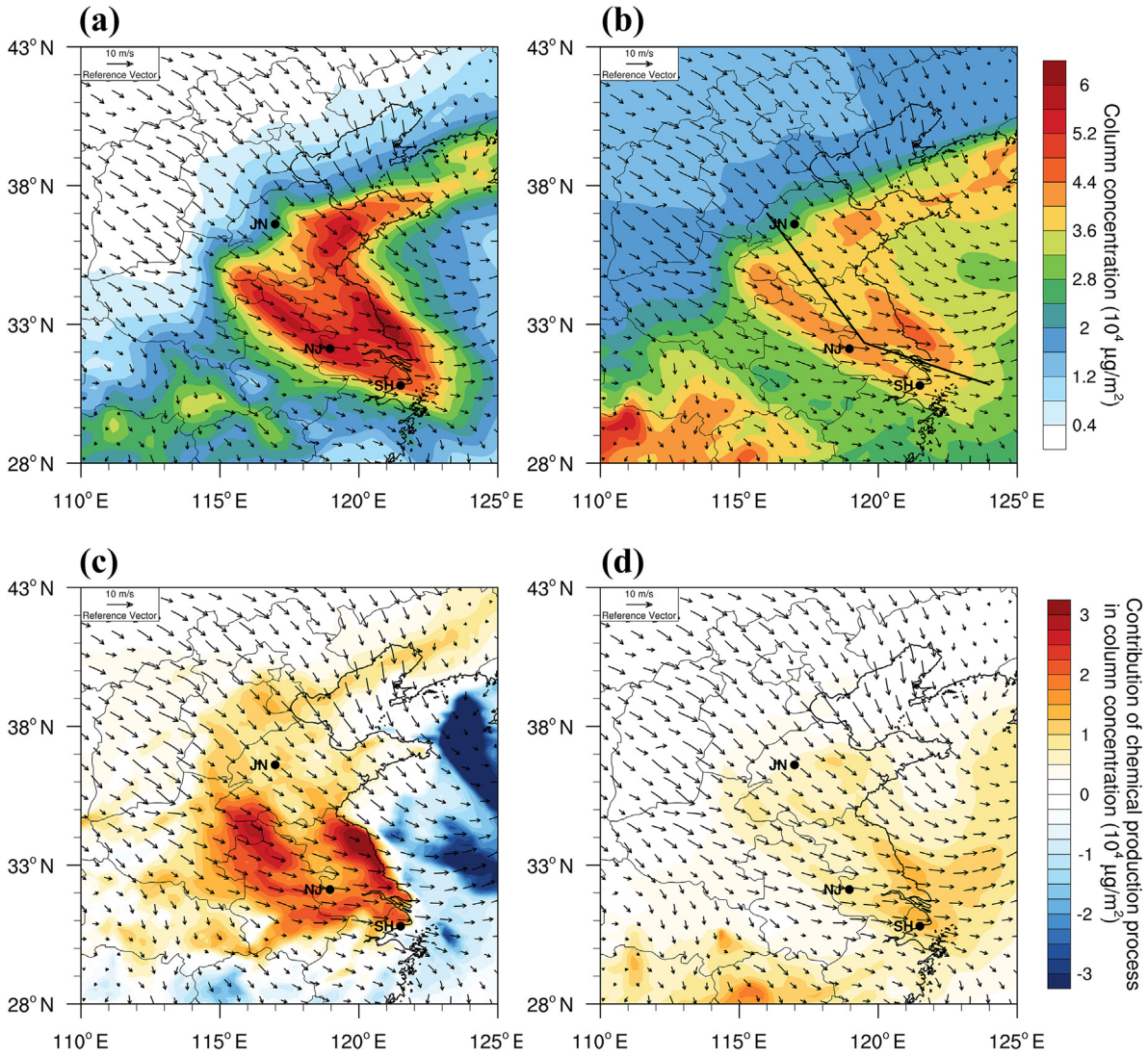

Fig. 9. Spatial distribution of the averaged column concentration during case 2. (a) NO_3^- column, (b) SO_4^{2-} column, (c) Column of NO_3^- from chemical production process, (d) Column of SO_4^{2-} from chemical production process. The black solid line in panel b denotes the location of the vertical cross section shown in Fig. 10. The location of Jinan, Nanjing and Shanghai are marked in black dots.

investigate the reasons why the chemical formation process decreased NO_3^- concentration at sea.

During the two cases, the spatial pattern of 2-m temperature in Fig. 12a indicated that the mean temperature on the ocean was higher than that of the land on the same latitude and the temperature in eastern China had a certain extent warming during the cold front episode, as displayed in Fig. 12b. Therefore, a relatively higher temperature at sea was unfavorable for the presence of NO_3^- in particulate phase. But the 2-m temperature pattern was not strictly distributed along the coastline, which mean that it was also affected by other factors.

NH_3 is a very important alkaline constituent in the atmosphere, which is a key precursor for neutralizing HNO_3 in the atmosphere to form NH_4NO_3. A comprehensive NH_3 emission inventory in China reveals that the most important emission sources are livestock excreta and fertilizer application and the regions with the highest emission rates are located in Central and Southwest China (Huang et al., 2012). As demonstrated in Fig. 12c and d, NH_3 was mainly distributed in the mainland, and the high concentration center was located in Henan province. The concentration of NH_3 over the sea was extremely low, and there was only a slight concentration near the coastline. Implying that the land presented NH_3-rich condition, but the sea was characterized as NH_3-poor condition. The neutralization of H_2SO_4 by NH_3 has been found to be preferred over the formation of NH_4NO_3 (Warneck, 1988). Thus, the formation of NH_4NO_3 in fine particles is usually under significantly neutralized or NH_3-rich conditions (Pathak et al., 2009). And the NH_3 concentration during case 2 was reduced compared to case 1, which may be explained by the conclusion mentioned above that the cold fronts carried both aerosols and gaseous precursors, and more NH_3 reacted with acidic species to form the major inorganic components of fine particulate matters.

Deposition is one of the main physical mechanisms of pollutants in the process of transport, and it is also the main process of pollutants removal in the air. The wet deposition process of pollutants falling to the ground with precipitation only occurs in a certain space and time, and the deposition amount is relatively concentrated. In the absence of precipitation, due to turbulent transport and gravity, pollutants are continuously absorbed by the underlying surface (including land surface, water surface and vegetation) when they are transported and diffused in the atmosphere, forming a continuous process of migration to the ground, which is called dry deposition. No precipitation occurred during the two cases in this study. The highly reactive and soluble nature of gaseous HNO_3 leads to large rates of deposition, approaching the maximum rates of deposition limited by turbulent exchange when each molecule arriving at terrestrial surface is immediately absorbed at the

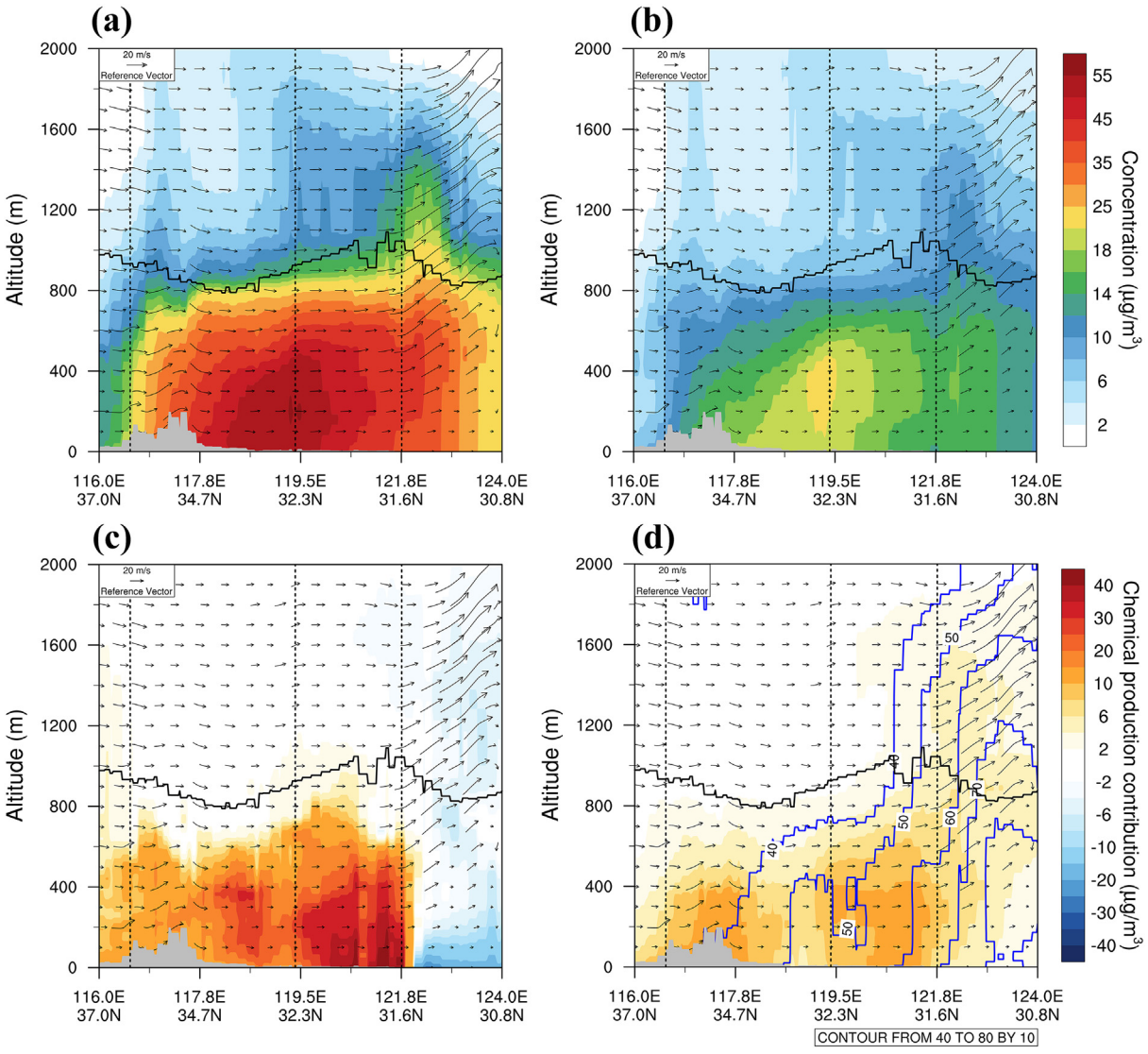

Fig. 10. Vertical cross section of (a) NO_3^- and (b) SO_4^{2-} averaged concentration during case 2, and the contribution of chemical production process on the vertical cross section of (c) NO_3^- and (d) SO_4^{2-} corresponding to Fig. 10a and b, in-plane wind vectors (arrows) where the vertical speed was multiplied by a factor of 1800, and planetary boundary layer height (black solid line). Blue lines in (d) outline RH. The corresponding location of Jinan, Nanjing and Shanghai are indicated as dashed black lines.

surface (Fowler et al., 2009; Sun et al., 2017). The difference in land-sea distribution of HNO_3 was not as obvious as NH_3, with a certain concentration both on land and sea, but the dry deposition at sea was significantly higher than that on land (Fig. 12e and f). Overall, the relative high temperature, the NH_3-poor condition and the large dry deposition of HNO_3 over the sea area did not facilitate the gas-to-particle partitioning, so the chemical formation process contributed negatively to NO_3^- concentration on the sea.

4. Conclusions

Eastern China has been facing severe winter haze pollution due mainly to secondary aerosol. To clearly understand the chemical formation and accumulation of main secondary composition SNA under typical synoptic weather conditions in this region, we conducted one-month simultaneous measurements on both meteorology and aerosol composition at multiple cities in late 2017. In addition, a fully coupled meteorology-chemistry model WRF-Chem with improved diagnose scheme was applied to shed more lights on SNA spatiotemporal characteristics and relative importance of different physical and chemical processes. The evaluation of simulation through ground-based observations shows that the model generally captured spatial patterns and temporal variations of meteorological parameters, $PM_{2.5}$ and its major chemical composition (SO_4^{2-}, NO_3^- and NH_4^+). SNA aerosols accounted for 41%, 44%, and 46% of $PM_{2.5}$ monthly in Jinan, Nanjing and Shanghai, with the fractions ranging from 6 to 13% in SO_4^{2-}, 22–26% in NO_3^- and 10–11% in NH_4^+, respectively. The Yangtze River Delta (YRD) of China is mainly affected by two kinds of synoptic systems in winter: one is the stable condition under the control of high pressure, and the other one is the cold front system ahead of the southward Siberian anticyclone. The averaged column concentration and chemical production of NO_3^- were in the range of 18.4–44.1 mg/m^2 and 14.1–14.7 mg/m^2 over the YRD region during two cases. And the corresponding range for SO_4^{2-} were 19.9–37.1 mg/m^2 and 3.2–8.7 mg/m^2, respectively.

The results show that the YRD region was slightly polluted during stable period, and the main source of pollutants at this time was local emissions. Whereas the cold front system moved southward, it carried the pollutants from the upwind areas, which would deteriorate air quality in the downwind areas, leading to heavy pollution in the YRD region. Our estimation indicated that the processes dominated the pollution of SNA were chemical formation during stable condition and advection

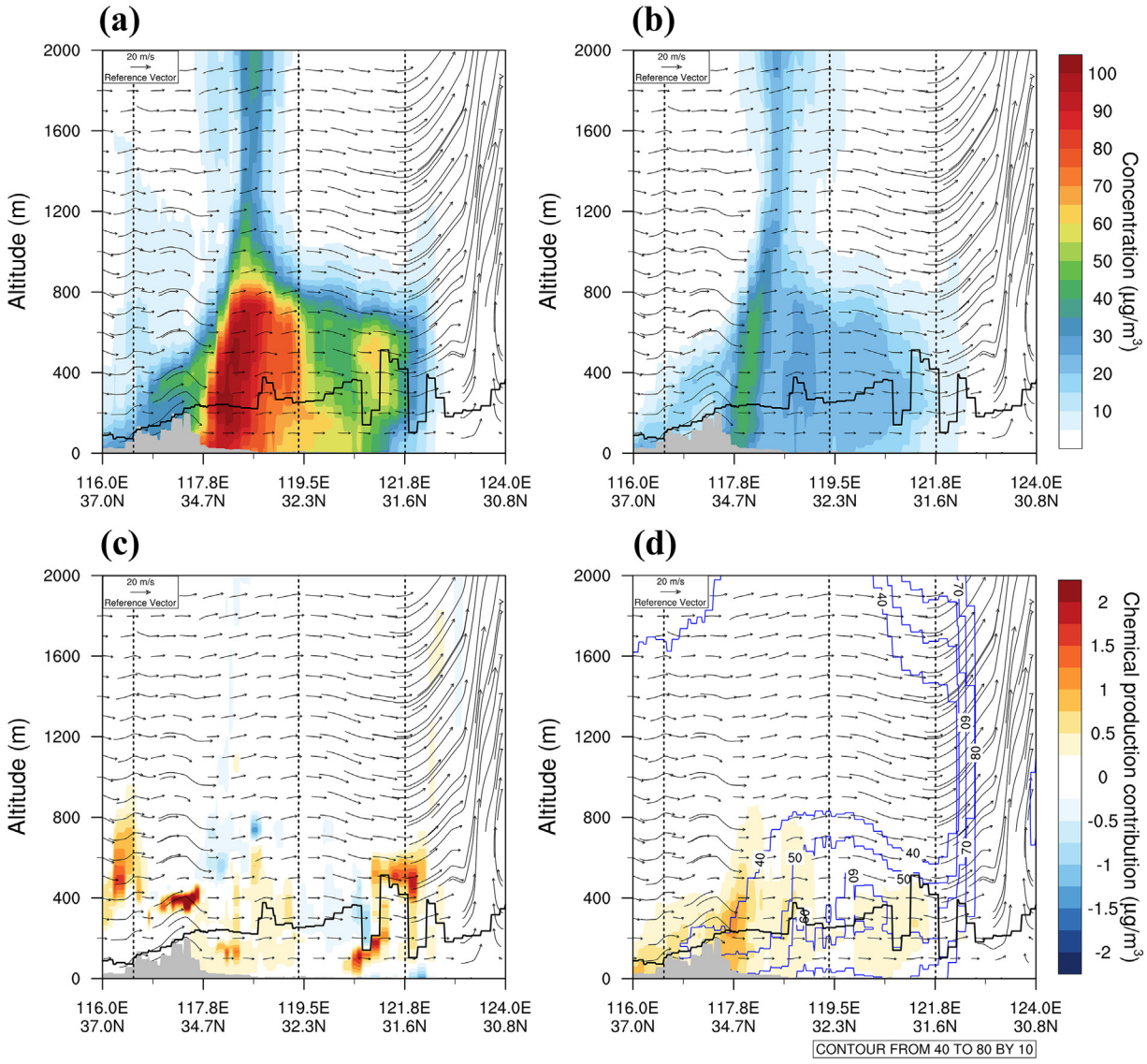

Fig. 11. Vertical cross section of (a) NO_3^- and (b) SO_4^{2-} concentration at 03:00 LT 24 December during case 2, and the hourly contribution of chemical production process on the vertical cross section of (c) NO_3^- and (d) SO_4^{2-} corresponding to panels a and b, in-plane wind vectors (arrows) where the vertical speed was multiplied by a factor of 1800, and planetary boundary layer height (black solid line). Blue lines in (d) outline RH. The corresponding location of Jinan, Nanjing and Shanghai are indicated as dashed black lines.

transport during cold frontal episode, contributing approximately 61% and 85% over the center of the YRD. When comparing the contribution of chemical production process to SNA on the spatial distribution under two different weather systems, the chemical production under stable weather (61.3%) contributed more to the column concentration than under the influence of cold front (14.8%) in terms of relative contribution ratio, but for the values of absolute contribution, it was the opposite. However, the photochemical activities were weakened during the pollution episode, so the contribution of gas-phase oxidation pathway to aerosol formation was limited. In addition, the emission inventory was fixed, i.e. the emission of local sources remained unchanged, and the heterogeneous chemical processes considered in the model were relatively simple, thus implying that the cold front carried both aerosols and gaseous precursors to the downstream, and the chemical conversion processes in the transport pathway led to the increase in the absolute contribution values. As for the characteristics of vertical structure, high concentrations of SNA and their gaseous precursors appeared near the surface in stable condition, while the altitudes of high concentration center were higher under the influence of cold front. Besides, the vertical distribution of SNA significantly exceeded the boundary layer height along the transport pathway of cold front, indicating that the warm and polluted air mass was lifted to the free troposphere by the upward motion ahead of the frontal zone. The chemical formation mainly occurred within the PBL, and also occurred above the top of the boundary layer during the transport process. The large values of chemical contribution were distributed in the downwind region along the city clusters from Nanjing to Shanghai, which included the chemical conversion of local emissions and the transported gaseous precursors from upstream. There was a significant difference in land-sea distribution of chemical formation contribution to NO_3^-, with positive contribution on land and negative contribution at sea. The relatively high temperature, the NH_3-poor condition and the large dry deposition of HNO_3 over the sea area were factors that impede the gas-to-particle partitioning, leading to the loss of nitrate aerosol.

CRediT authorship contribution statement

Tianyi Wang: Formal analysis, Methodology, Visualization, Writing - review & editing.**Xin Huang:**Methodology, Investigation,

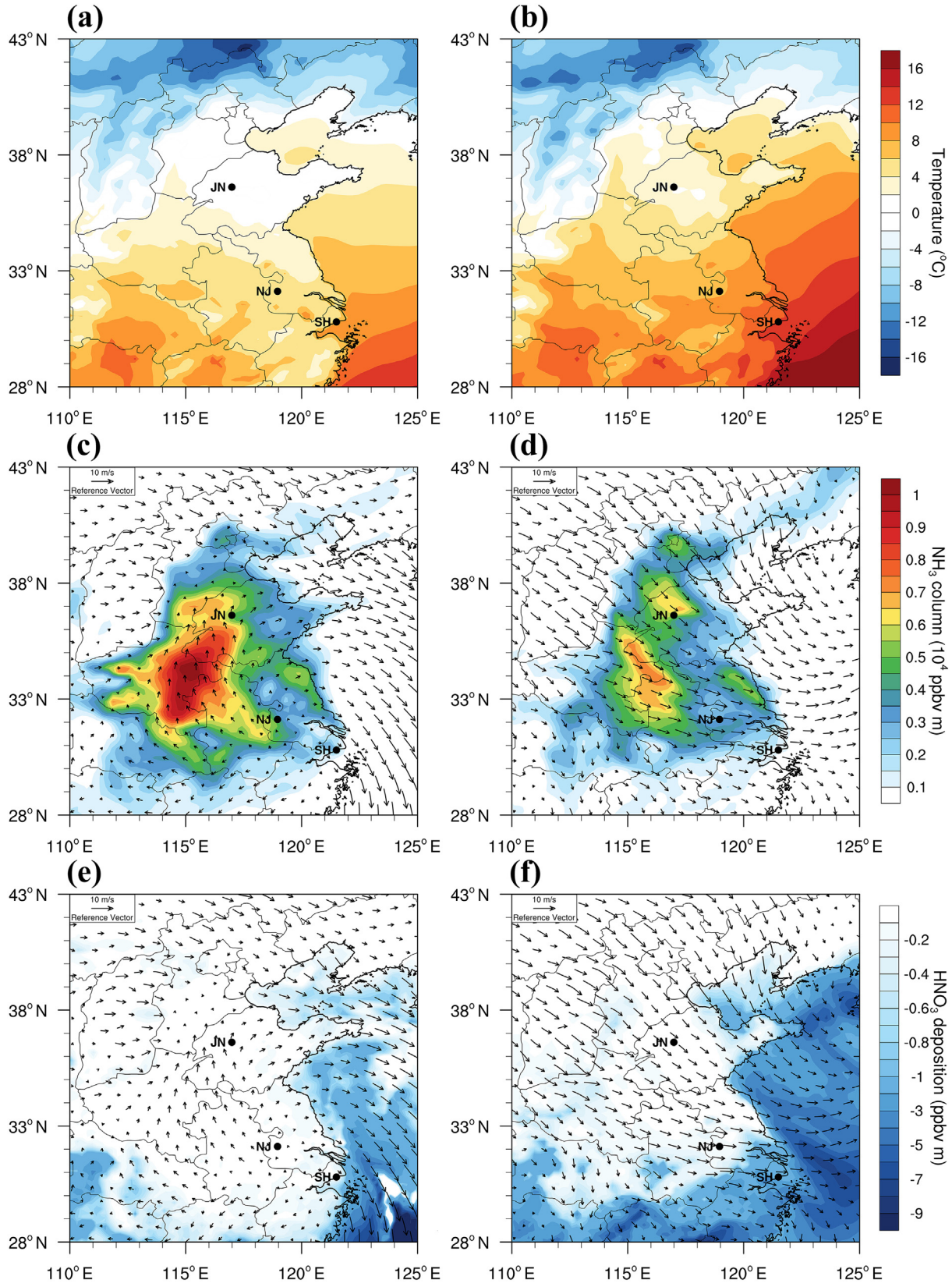

Fig. 12. Mean 2-m temperature during (a) case 1 and (b) case 2. Spatial distribution of the averaged NH_3 column during (c) case 1 and (d) case 2. Total dry deposition of HNO_3 during (e) case 1 and (f) case 2.

Writing - review & editing.**Zilin Wang:**Methodology, Visualization. **Yuliang Liu:**Data curation.**Derong Zhou:**Methodology, Data curation.**Ke Ding:**Methodology, Visualization. **Hongyue Wang:**Visualization.**Ximeng Qi:**Formal analysis, Data curation.**Aijun Ding:**Conceptualization, Supervision, Funding acquisition.

Declaration of competing interest

The authors declare that they have no known competing financial interests or personal relationships that could have appeared to influence the work reported in this paper.

Acknowledgments

This work was supported by the Ministry of Science and Technology of the People's Republic of China (2018YFC0213800, 2016YFC0200500), the National Natural Science Foundation of China (91544231, 41725020, 91744311, and 41422504) and the international cooperation project of Jiangsu Provincial Science and Technology Agency (BZ2017066). The numerical modeling was conducted on computing facilities at the High Performance Computing Centering (HPCC) at Nanjing University.

Appendix A. Supplementary data

Supplementary data to this article can be found online at https://doi.org/10.1016/j.scitotenv.2020.138888.

References

Adams, P.J., Seinfeld, J.H., Koch, D.M., 1999. Global concentrations of tropospheric sulfate, nitrate, and ammonium aerosol simulated in a general circulation model. J. Geophys. Res.-Atmos. 104, 13791–13823.
Alexander, B., Hastings, M.G., Allman, D.J., Dachs, J., Thornton, J.A., Kunasek, S.A., 2009. Quantifying atmospheric nitrate formation pathways based on a global model of the oxygen isotopic composition (delta O-17) of atmospheric nitrate. Atmos. Chem. Phys. 9, 5043–5056.
Ansari, A.S., Pandis, S.N., 2000. The effect of metastable equilibrium states on the partitioning of nitrate between the gas and aerosol phases. Atmos. Environ. 34, 157–168.
Brown, S.S., Stark, H., Ryerson, T.B., Williams, E.J., Nicks, D.K., Trainer, M., et al., 2003. Nitrogen oxides in the nocturnal boundary layer: simultaneous in situ measurements of NO3, N2O5, NO2, NO, and O-3. J. Geophys. Res.-Atmos. 108.
Cao, J.-J., Shen, Z.-X., Chow, J.C., Watson, J.G., Lee, S.-C., Tie, X.-X., et al., 2012a. Winter and summer PM2.5 chemical compositions in fourteen Chinese cities. J. Air Waste Manage. Assoc. 62, 1214–1226.
Cao, J., Xu, H., Xu, Q., Chen, B., Kan, H., 2012b. Fine particulate matter constituents and cardiopulmonary mortality in a heavily polluted Chinese city. Environ. Health Perspect. 120, 373–378.
Carslaw, K.S., Boucher, O., Spracklen, D.V., Mann, G.W., Rae, J.G.L., Woodward, S., et al., 2010. A review of natural aerosol interactions and feedbacks within the earth system. Atmos. Chem. Phys. 10, 1701–1737.
Chan, C.K., Yao, X., 2008. Air pollution in mega cities in China. Atmos. Environ. 42, 1–42.
Cheng, W.Y.Y., Steenburgh, W.J., 2005. Evaluation of surface sensible weather forecasts by the WRF and the eta models over the western United States. Weather Forecast. 20, 812–821.
Cheng, Y., Zheng, G., Wei, C., Mu, Q., Zheng, B., Wang, Z., et al., 2016. Reactive nitrogen chemistry in aerosol water as a source of sulfate during haze events in China. Sci. Adv. 2.
Dandou, A., Tombrou, M., Akylas, E., Soulakellis, N., Bossioli, E., 2005. Development and evaluation of an urban parameterization scheme in the Penn State/NCAR mesoscale model (MM5). J. Geophys. Res. 110.
Ding, A., Wang, T., Xue, L., Gao, J., Stohl, A., Lei, H., et al., 2009. Transport of North China air pollution by midlatitude cyclones: case study of aircraft measurements in summer 2007. J. Geophys. Res.-Atmos. 114.
Ding, A., Wang, T., Fu, C., 2013a. Transport characteristics and origins of carbon monoxide and ozone in Hong Kong, South China. J. Geophys. Res.-Atmos. 118, 9475–9488.
Ding, A.J., Fu, C.B., Yang, X.Q., Sun, J.N., Petaja, T., Kerminen, V.M., et al., 2013b. Intense atmospheric pollution modifies weather: a case of mixed biomass burning with fossil fuel combustion pollution in eastern China. Atmos. Chem. Phys. 13, 10545–10554.
Ding, A.J., Fu, C.B., Yang, X.Q., Sun, J.N., Zheng, L.F., Xie, Y.N., et al., 2013c. Ozone and fine particle in the western Yangtze River Delta: an overview of 1 yr data at the SORPES station. Atmos. Chem. Phys. 13, 5813–5830.
Ding, A., Nie, W., Huang, X., Chi, X., Sun, J., Kerminen, V.-M., et al., 2016. Long-term observation of air pollution-weather/climate interactions at the SORPES station: a review and outlook. Front. Environ. Sci. Eng. 10.
Ding, A., Huang, X., Nie, W., Chi, X., Xu, Z., Zheng, L., et al., 2019. Significant reduction of PM2.5 in eastern China due to regional-scale emission control: evidence from SORPES in 2011–2018. Atmos. Chem. Phys. 19, 11791–11801.
Dong, X., Gao, Y., Fu, J.S., Li, J., Huang, K., Zhuang, G., et al., 2013. Probe into gaseous pollution and assessment of air quality benefit under sector dependent emission control strategies over megacities in Yangtze River Delta, China. Atmos. Environ. 79, 841–852.
Elser, M., Huang, R.-J., Wolf, R., Slowik, J.G., Wang, Q., Canonaco, F., et al., 2016. New insights into PM2.5 chemical composition and sources in two major cities in China during extreme haze events using aerosol mass spectrometry. Atmos. Chem. Phys. 16, 3207–3225.
Fowler, D., Pilegaard, K., Sutton, M.A., Ambus, P., Raivonen, M., Duyzer, J., et al., 2009. Atmospheric composition change: ecosystems-atmosphere interactions. Atmos. Environ. 43, 5193–5267.
Gao, Y., Shan, H., Zhang, S., Sheng, L., Li, J., Zhang, J., et al., 2020. Characteristics and sources of PM2.5 with focus on two severe pollution events in a coastal city of Qingdao, China. Chemosphere 247, 125861.
Geng, G., Zhang, Q., Tong, D., Li, M., Zheng, Y., Wang, S., et al., 2017. Chemical composition of ambient PM2.5 over China and relationship to precursor emissions during 2005–2012. Atmos. Chem. Phys. 17, 9187–9203.
Grell, G., Freitas, S.R., Stuefer, M., Fast, J., 2011. Inclusion of biomass burning in WRF-Chem: impact of wildfires on weather forecasts. Atmos. Chem. Phys. 11, 5289–5303.
Guo, S., Hu, M., Zamora, M.L., Peng, J., Shang, D., Zheng, J., et al., 2014. Elucidating severe urban haze formation in China. Proc. Natl. Acad. Sci. U. S. A. 111, 17373–17378.
Guo, H., Weber, R.J., Nenes, A., 2017. High levels of ammonia do not raise fine particle pH sufficiently to yield nitrogen oxide-dominated sulfate production. Sci. Rep. 7, 12109.
Harris, E., Sinha, B., Pinxteren, D., Tilgner, A., Fomba, K., Schneider, J., et al., 2013. Enhanced role of transition metal ion catalysis during in-cloud oxidation of SO2. Science (New York, N.Y.) 340, 727–730.
Harrison, R.M., Yin, J.X., 2000. Particulate matter in the atmosphere: which particle properties are important for its effects on health? Sci. Total Environ. 249, 85–101.
Held, A., Hinz, K.P., Trimborn, A., Spengler, B., Klemm, O., 2002. Chemical classes of atmospheric aerosol particles at a rural site in Central Europe during winter. J. Aerosol Sci. 33, 581–594.
Huang, X., Song, Y., Li, M., Li, J., Huo, Q., Cai, X., et al., 2012. A high-resolution ammonia emission inventory in China. Glob. Biogeochem. Cycles 26.
Huang, K., Fu, J.S., Gao, Y., Dong, X., Zhuang, G., Lin, Y., 2014a. Role of sectoral and multi-pollutant emission control strategies in improving atmospheric visibility in the Yangtze River Delta, China. Environ. Pollut. 184, 426–434.
Huang, R.-J., Zhang, Y., Bozzetti, C., Ho, K.-F., Cao, J.-J., Han, Y., et al., 2014b. High secondary aerosol contribution to particulate pollution during haze events in China. Nature 514, 218–222.
Huang, X., Song, Y., Zhao, C., Li, M., Zhu, T., Zhang, Q., et al., 2014c. Pathways of sulfate enhancement by natural and anthropogenic mineral aerosols in China. J. Geophys. Res.-Atmos. 119, 14165–14179.
Huang, X., Song, Y., Zhao, C., Cai, X., Zhang, H., Zhu, T., 2015. Direct radiative effect by multicomponent aerosol over China. J. Clim. 28, 3472–3495.
Huang, X., Ding, A., Liu, L., Liu, Q., Ding, K., Niu, X., et al., 2016. Effects of aerosol-radiation interaction on precipitation during biomass-burning season in East China. Atmos. Chem. Phys. 16, 10063–10082.
Huang, X., Wang, Z., Ding, A., 2018. Impact of aerosol-PBL interaction on haze pollution: multiyear observational evidences in North China. Geophys. Res. Lett. 45, 8596–8603.
Jiang, C., Wang, H., Zhao, T., Li, T., Che, H., 2015. Modeling study of PM2.5 pollutant transport across cities in China's Jing-Jin-Ji region during a severe haze episode in December 2013. Atmos. Chem. Phys. 15, 5803–5814.
Jung, J., Lee, H., Kim, Y.J., Liu, X., Zhang, Y., Hu, M., et al., 2009. Optical properties of atmospheric aerosols obtained by in situ and remote measurements during 2006 campaign of air quality research in Beijing (CAREBeijing-2006). J. Geophys. Res.-Atmos. 114.
Kang, H., Zhu, B., Gao, J., He, Y., Wang, H., Su, J., et al., 2019. Potential impacts of cold frontal passage on air quality over the Yangtze River Delta, China. Atmos. Chem. Phys. 19, 3673–3685.
Kulmala, M., Suni, T., Lehtinen, K.E.J., Dal Maso, M., Boy, M., Reissell, A., et al., 2004. A new feedback mechanism linking forests, aerosols, and climate. Atmos. Chem. Phys. 4, 557–562.
Kunen, S.M., Lazrus, A.L., Kok, G.L., Heikes, B.G., 1983. Aqueous oxidation of SO2 by hydrogen peroxide. J. Geophys. Res. Oceans 88, 3671–3674.
Li, J., Wang, Z., Huang, H., Hu, M., Meng, F., Sun, Y., et al., 2013. Assessing the effects of trans-boundary aerosol transport between various city clusters on regional haze episodes in spring over East China. Tellus Ser. B Chem. Phys. Meteorol. 65.
Li, J., Chen, H., Li, Z., Wang, P., Cribb, M., Fan, X., 2015a. Low-level temperature inversions and their effect on aerosol condensation nuclei concentrations under different large-scale synoptic circulations. Adv. Atmos. Sci. 32, 898–908.
Li, J., Fu, Q., Huo, J., Wang, D., Yang, W., Bian, Q., et al., 2015b. Tethered balloon-based black carbon profiles within the lower troposphere of Shanghai in the 2013 East China smog. Atmos. Environ. 123, 327–338.
Li, G., Bei, N., Cao, J., Huang, R., Wu, J., Feng, T., et al., 2017. A possible pathway for rapid growth of sulfate during haze days in China. Atmos. Chem. Phys. 17, 3301–3316.
Li, M., Wang, T., Xie, M., Li, S., Zhuang, B., Huang, X., et al., 2019. Formation and evolution mechanisms for two extreme haze episodes in the Yangtze River Delta Region of China during winter 2016. J. Geophys. Res.-Atmos. 124, 3607–3623.
Liu, H.Y., Jacob, D.J., Bey, I., Yantosca, R.M., Duncan, B.N., Sachse, G.W., 2003. Transport pathways for Asian pollution outflow over the Pacific: interannual and seasonal variations. J. Geophys. Res.-Atmos. 108.
Liu, X.G., Li, J., Qu, Y., Han, T., Hou, L., Gu, J., et al., 2013. Formation and evolution mechanism of regional haze: a case study in the megacity Beijing, China. Atmos. Chem. Phys. 13, 4501–4514.
Liu, Y., Nie, W., Xu, Z., Wang, T., Wang, R., Li, Y., et al., 2019. Semi-quantitative understanding of source contribution to nitrous acid (HONO) based on 1 year of continuous observation at the SORPES station in eastern China. Atmos. Chem. Phys. 19, 13289–13308.
Lohmann, U., Feichter, J., 2005. Global indirect aerosol effects: a review. Atmos. Chem. Phys. 5, 715–737.
Lu, Z., Zhang, Q., Streets, D.G., 2011. Sulfur dioxide and primary carbonaceous aerosol emissions in China and India, 1996–2010. Atmos. Chem. Phys. 11, 9839–9864.
Matsui, H., Koike, M., Kondo, Y., Takegawa, N., Kita, K., Miyazaki, Y., et al., 2009. Spatial and temporal variations of aerosols around Beijing in summer 2006: model evaluation and source apportionment. J. Geophys. Res.-Atmos. 114.

Meng, Z.Y., Seinfeld, J.H., 1994. On the source of the submicrometer droplet mode of urban and regional aerosols. Aerosol Sci. Technol. 20, 253–265.
Meng, Z., Xie, Y., Jia, S., Zhang, R., Lin, W., Xu, X., et al., 2015. Characteristics of atmospheric ammonia at Gucheng, a rural site on North China plain in summer of 2013. J. Appl. Meteorol. Sci. 26, 141–150.
Ming, L., Jin, L., Li, J., Fu, P., Yang, W., Liu, D., et al., 2017. PM2.5 in the Yangtze River Delta, China: chemical compositions, seasonal variations, and regional pollution events. Environ. Pollut. 223, 200–212.
Moelders, N., Tran, H.N.Q., Cahill, C.F., Leelasakultum, K., Tran, T.T., 2012. Assessment of WRF/Chem PM2.5 forecasts using mobile and fixed location data from the Fairbanks, Alaska winter 2008/09 field campaign. Atmos. Pollut. Res. 3, 180–191.
Nie, W., Ding, A.J., Xie, Y.N., Xu, Z., Mao, H., Kerminen, V.M., et al., 2015. Influence of biomass burning plumes on HONO chemistry in eastern China. Atmos. Chem. Phys. 15, 1147–1159.
Pathak, R.K., Wu, W.S., Wang, T., 2009. Summertime PM2.5 ionic species in four major cities of China: nitrate formation in an ammonia-deficient atmosphere. Atmos. Chem. Phys. 9, 1711–1722.
Pinder, R.W., Adams, P.J., Pandis, S.N., 2007. Ammonia emission controls as a cost-effective strategy for reducing atmospheric particulate matter in the eastern United States. Environ. Sci. Technol. 41, 380–386.
Pope III, C.A., Dockery, D.W., 2006. Health effects of fine particulate air pollution: lines that connect. J. Air Waste Manage. Assoc. 56, 709–742.
Qi, X., Ding, A., Nie, W., Chi, X., Huang, X., Xu, Z., et al., 2019. Direct measurement of new particle formation based on tethered airship around the top of the planetary boundary layer in eastern China. Atmos. Environ. 209, 92–101.
Querol, X., Alastuey, A., Ruiz, C.R., Artinano, B., Hansson, H.C., Harrison, R.M., et al., 2004. Speciation and origin of PM10 and PM2.5 in selected European cities. Atmos. Environ. 38, 6547–6555.
Seinfeld, J.H., Pandis, S.N., 2016. Atmospheric Chemistry and Physics: From Air Pollution to Climate Change. Wiley.
Shen, Y., Virkkula, A., Ding, A., Wang, J., Chi, X., Nie, W., et al., 2018. Aerosol optical properties at SORPES in Nanjing, East China. Atmos. Chem. Phys. 18, 5265–5292.
Stein, A.F., Draxler, R.R., Rolph, G.D., Stunder, B.J.B., Cohen, M.D., Ngan, F., 2015. NOAA's hysplit atmospheric transport and dispersion modeling system. Bull. Am. Meteorol. Soc. 96, 2059–2077.
Sun, Y., Jiang, Q., Wang, Z., Fu, P., Li, J., Yang, T., et al., 2014. Investigation of the sources and evolution processes of severe haze pollution in Beijing in January 2013. J. Geophys. Res.-Atmos. 119, 4380–4398.
Sun, J., Fu, J.S., Lynch, J.A., Huang, K., Gao, Y., 2017. Climate-driven exceedance of total (wet plus dry) nitrogen (N) plus sulfur (S) deposition to forest soil over the conterminous US. Earths Future 5, 560–576.
Sun, P., Nie, W., Chi, X., Xie, Y., Huang, X., Xu, Z., et al., 2018. Two years of online measurement of fine particulate nitrate in the western Yangtze River Delta: influences of thermodynamics and N2O5 hydrolysis. Atmos. Chem. Phys. 18, 17177–17190.
Tan, J.-H., Duan, J.-C., Chen, D.-H., Wang, X.-H., Guo, S.-J., Bi, X.-H., et al., 2009. Chemical characteristics of haze during summer and winter in Guangzhou. Atmos. Res. 94, 238–245.
Tang, L., Yu, H., Ding, A., Zhang, Y., Qin, W., Wang, Z., et al., 2016. Regional contribution to PM1 pollution during winter haze in Yangtze River Delta, China. Sci. Total Environ. 541, 161–166.
Thornton, J.A., Braban, C.F., Abbatt, J.P.D., 2003. N2O5 hydrolysis on sub-micron organic aerosols: the effect of relative humidity, particle phase, and particle size. Phys. Chem. Chem. Phys. 5, 4593–4603.
Tie, X., Cao, J., 2009. Aerosol pollution in China: present and future impact on environment. Particuology 7, 426–431.
Tuccella, P., Curci, G., Visconti, G., Bessagnet, B., Menut, L., Park, R.J., 2012. Modeling of gas and aerosol with WRF/Chem over Europe: evaluation and sensitivity study. J. Geophys. Res.-Atmos. 117.
Wang, Y., Zhuang, G., Sun, Y., An, Z., 2006. The variation of characteristics and formation mechanisms of aerosols in dust, haze, and clear days in Beijing. Atmos. Environ. 40, 6579–6591.
Wang, Y., Zhang, Q.Q., He, K., Zhang, Q., Chai, L., 2013. Sulfate-nitrate-ammonium aerosols over China: response to 2000–2015 emission changes of sulfur dioxide, nitrogen oxides, and ammonia. Atmos. Chem. Phys. 13, 2635–2652.
Wang, Y., Yao, L., Wang, L., Liu, Z., Ji, D., Tang, G., et al., 2014a. Mechanism for the formation of the January 2013 heavy haze pollution episode over central and eastern China. Sci. China Ser. D Earth Sci. 57, 14–25.
Wang, Y., Zhang, Q., Jiang, J., Zhou, W., Wang, B., He, K., et al., 2014b. Enhanced sulfate formation during China's severe winter haze episode in January 2013 missing from current models. J. Geophys. Res.-Atmos. 119.
Wang, M., Cao, C., Li, G., Singh, R.P., 2015a. Analysis of a severe prolonged regional haze episode in the Yangtze River Delta, China. Atmos. Environ. 102, 112–121.
Wang, Y.H., Liu, Z.R., Zhang, J.K., Hu, B., Ji, D.S., Yu, Y.C., et al., 2015b. Aerosol physicochemical properties and implications for visibility during an intense haze episode during winter in Beijing. Atmos. Chem. Phys. 15, 3205–3215.
Wang, G., Zhang, R., Gomez, M.E., Yang, L., Zamora, M.L., Hu, M., et al., 2016. Persistent sulfate formation from London fog to Chinese haze. Proc. Natl. Acad. Sci. U. S. A. 113, 13630–13635.
Wang, J., Zhao, B., Wang, S., Yang, F., Xing, J., Morawska, L., et al., 2017a. Particulate matter pollution over China and the effects of control policies. Sci. Total Environ. 584, 426–447.
Wang, Y.C., Huang, R.J., Ni, H.Y., Chen, Y., Wang, Q.Y., Li, G.H., et al., 2017b. Chemical composition, sources and secondary processes of aerosols in Baoji city of northwest China. Atmos. Environ. 158, 128–137.
Wang, H., Tian, M., Chen, Y., Shi, G., Liu, Y., Yang, F., et al., 2018a. Seasonal characteristics, formation mechanisms and source origins of PM2.5 in two megacities in Sichuan Basin, China. Atmos. Chem. Phys. 18, 865–881.
Wang, Z., Huang, X., Ding, A., 2018b. Dome effect of black carbon and its key influencing factors: a one-dimensional modelling study. Atmos. Chem. Phys. 18, 2821–2834.
Wang, Z., Huang, X., Ding, A., 2019. Optimization of vertical grid setting for air quality modelling in China considering the effect of aerosol-boundary layer interaction. Atmos. Environ. 210, 1–13.
Warneck, P., 1988. Chemistry of the natural atmosphere. International Geophysics. 41. Academic Press Inc, Orlando FL, pp. 1–70.
Wen, L., Xue, L., Wang, X., Xu, C., Chen, T., Yang, L., et al., 2018. Summertime fine particulate nitrate pollution in the North China Plain: increasing trends, formation mechanisms and implications for control policy. Atmos. Chem. Phys. 18, 11261–11275.
Xie, Y., Ding, A., Nie, W., Mao, H., Qi, X., Huang, X., et al., 2015. Enhanced sulfate formation by nitrogen dioxide: implications from in situ observations at the SORPES station. J. Geophys. Res.-Atmos. 120, 12679–12694.
Xu, J., Ma, J.Z., Zhang, X.L., Xu, X.B., Xu, X.F., Lin, W.L., et al., 2011. Measurements of ozone and its precursors in Beijing during summertime: impact of urban plumes on ozone pollution in downwind rural areas. Atmos. Chem. Phys. 11, 12241–12252.
Xu, Z., Huang, X., Nie, W., Chi, X., Xu, Z., Zheng, L., et al., 2017. Influence of synoptic condition and holiday effects on VOCs and ozone production in the Yangtze River Delta region, China. Atmos. Environ. 168, 112–124.
Xu, Z., Huang, X., Nie, W., Shen, Y., Zheng, L., Xie, Y., et al., 2018. Impact of biomass burning and vertical mixing of residual-layer aged plumes on ozone in the Yangtze River Delta, China: a tethered-balloon measurement and modeling study of a multiday ozone episode. J. Geophys. Res.-Atmos. 123, 11786–11803.
Yahya, K., Wang, K., Gudoshava, M.L., Glotfelty, T., Zhang, Y., 2015. Application of WRF/Chem over North America under the AQMEII phase 2: part I. comprehensive evaluation of 2006 simulation. Atmos. Environ. 115, 733–755.
Yang, F., Tan, J., Zhao, Q., Du, Z., He, K., Ma, Y., et al., 2011. Characteristics of PM2.5 speciation in representative megacities and across China. Atmos. Chem. Phys. 11, 5207–5219.
Yang, X., Zhao, C., Zhou, L., Li, Z., Cribb, M., Yang, S., 2018. Wintertime cooling and a potential connection with transported aerosols in Hong Kong during recent decades. Atmos. Res. 211, 52–61.
Ying, Q., Wu, L., Zhang, H., 2014. Local and inter-regional contributions to PM2.5 nitrate and sulfate in China. Atmos. Environ. 94, 582–592.
Zhang, Q., Jimenez, J.L., Worsnop, D.R., Canagaratna, M., 2007. A case study of urban particle acidity and its influence on secondary organic aerosol. Environ. Sci. Technol. 41, 3213–3219.
Zhang, Q., Streets, D.G., Carmichael, G.R., He, K.B., Huo, H., Kannari, A., et al., 2009. Asian emissions in 2006 for the NASA INTEX-B mission. Atmos. Chem. Phys. 9, 5131–5153.
Zhang, Y., Wen, X.Y., Jang, C.J., 2010. Simulating chemistry-aerosol-cloud-radiation-climate feedbacks over the continental US using the online-coupled weather research forecasting model with chemistry (WRF/Chem). Atmos. Environ. 44, 3568–3582.
Zhang, J.P., Zhu, T., Zhang, Q.H., Li, C.C., Shu, H.L., Ying, Y., et al., 2012a. The impact of circulation patterns on regional transport pathways and air quality over Beijing and its surroundings. Atmos. Chem. Phys. 12, 5031–5053.
Zhang, R., Khalizov, A., Wang, L., Hu, M., Xu, W., 2012b. Nucleation and growth of nanoparticles in the atmosphere. Chem. Rev. 112, 1957–2011.
Zhang, X.Y., Wang, Y.Q., Niu, T., Zhang, X.C., Gong, S.L., Zhang, Y.M., et al., 2012c. Atmospheric aerosol compositions in China: spatial/temporal variability, chemical signature, regional haze distribution and comparisons with global aerosols. Atmos. Chem. Phys. 12, 779–799.
Zhang, R., Jing, J., Tao, J., Hsu, S.C., Wang, G., Cao, J., et al., 2013. Chemical characterization and source apportionment of PM2.5 in Beijing: seasonal perspective. Atmos. Chem. Phys. 13, 7053–7074.
Zhang, B., Wang, Y., Hao, J., 2015a. Simulating aerosol–radiation–cloud feedbacks on meteorology and air quality over eastern China under severe haze conditionsin winter. Atmos. Chem. Phys. 15, 2387–2404.
Zhang, R., Wang, G., Guo, S., Zamora, M.L., Ying, Q., Lin, Y., et al., 2015b. Formation of urban fine particulate matter. Chem. Rev. 115, 3803–3855.
Zhang, Y., Ding, A., Mao, H., Nie, W., Zhou, D., Liu, L., et al., 2016. Impact of synoptic weather patterns and inter-decadal climate variability on air quality in the North China plain during 1980–2013. Atmos. Environ. 124, 119–128.
Zhang, K., Wang, D., Bian, Q., Duan, Y., Zhao, M., Fei, D., et al., 2017. Tethered balloon-based particle number concentration, and size distribution vertical profiles within the lower troposphere of Shanghai. Atmos. Environ. 154, 141–150.
Zhang, K., Xiu, G., Zhou, L., Bian, Q., Duan, Y., Fei, D., et al., 2018. Vertical distribution of volatile organic compounds within the lower troposphere in late spring of Shanghai. Atmos. Environ. 186, 150–157.
Zhao, B., Wang, S., Dong, X., Wang, J., Duan, L., Fu, X., et al., 2013a. Environmental effects of the recent emission changes in China: implications for particulate matter pollution and soil acidification. Environ. Res. Lett. 8.
Zhao, X.J., Zhao, P.S., Xu, J., Meng, W., Pu, W.W., Dong, F., et al., 2013b. Analysis of a winter regional haze event and its formation mechanism in the North China plain. Atmos. Chem. Phys. 13, 5685–5696.
Zheng, G.J., Duan, F.K., Su, H., Ma, Y.L., Cheng, Y., Zheng, B., et al., 2015. Exploring the severe winter haze in Beijing: the impact of synoptic weather, regional transport and heterogeneous reactions. Atmos. Chem. Phys. 15, 2969–2983.
Zhou, D., Ding, K., Huang, X., Liu, L., Liu, Q., Xu, Z., et al., 2018. Transport, mixing and feedback of dust, biomass burning and anthropogenic pollutants in eastern Asia: a case study. Atmos. Chem. Phys. 18, 16345–16361.
Zhu, B., Su, J., Han, Z., Yin, C., Wang, T., 2010. Analysis of a serious air pollution event resulting from crop residue burning over Nanjing and surrounding regions. China Environ. Sci. 30, 585–592.
Zhu, X., Tang, G., Hu, B., Wang, L., Xin, J., Zhang, J., et al., 2016. Regional pollution and its formation mechanism over North China plain: a case study with ceilometer observations and model simulations. J. Geophys. Res.-Atmos. 121, 14574–14588.